On the emergence of macroscopic transport barriers from staircase structures

Arash Ashourvan and P. H. Diamond

Citation: Phys. Plasmas **24**, 012305 (2017); doi: 10.1063/1.4973660
View online: http://dx.doi.org/10.1063/1.4973660
View Table of Contents: http://aip.scitation.org/toc/php/24/1
Published by the American Institute of Physics

On the emergence of macroscopic transport barriers from staircase structures

Arash Ashourvan[1] and P. H. Diamond[2,3,4]
[1]*Princeton Plasma Physics Laboratory, PO Box 451, Princeton, New Jersey 08543, USA*
[2]*Center for Momentum Transport and Flow Organization, University of California San Diego, La Jolla, California 92093, USA*
[3]*Center for Energy Research, University of California San Diego, La Jolla, California 92093, USA*
[4]*Center for Astrophysics and Space Sciences (CASS) and Department of Physics, University of California San Diego, La Jolla, California 92093, USA*

(Received 30 June 2016; accepted 22 December 2016; published online 20 January 2017)

This paper presents a theory for the formation and evolution of coupled density staircases and zonal shear profiles in a simple model of drift-wave turbulence. Density, vorticity, and fluctuation potential enstrophy are the fields evolved in this system. Formation of staircase structures is due to inhomogeneous mixing of generalized potential vorticity (PV), resulting in the sharpening of density and vorticity gradients in some regions, and weakening them in others. When the PV gradients steepen, the density staircase structure develops into a lattice of mesoscale "jumps," and "steps," which are, respectively, the regions of local gradient steepening and flattening. The jumps merge and migrate in radius, leading to the development of macroscale profile structures from mesoscale elements. The positive feedback process, which drives the staircase formation occurs via a Rhines scale dependent mixing length. We present extensive studies of bifurcation physics of the *global* state, including results on the global flux-gradient relations (flux landscapes) predicted by the model. Furthermore, we demonstrate that, depending on the sources and boundary conditions, either a region of enhanced confinement, or a region with strong turbulence can form at the edge. This suggests that the profile self-organization is a *global* process, though one which can be described by a local, but nonlinear model. This model is the first to demonstrate how the mesoscale condensation of staircases leads to global states of enhanced confinement. *Published by AIP Publishing.*
[http://dx.doi.org/10.1063/1.4973660]

I. INTRODUCTION

Self-generated zonal flow (ZF) shears have been a topic of interest in the fusion community due to their important role in suppression of turbulent transport and triggering the development of the H-mode and internal transport barriers (ITBs)[1,2] (see Ref. 3 for a general review of the zonal flows). However, beyond magnetic fusion physics, quasi-periodic patterns of flows are ubiquitous in nature, especially in the planetary atmospheres (Earth,[4,5] Jupiter[6]). In these non-fusion examples, despite the different physics involved, the emergence of shear layers results from the central idea of positive feedback resulting from inhomogeneous turbulent mixing. This leads to the formation of regions with strong mixing and weak wave elasticity,[7] separated by interfaces with steepened potential vorticity (PV) gradients and sharpened flows. This process can be thought of as the *PV-Phillips effect*, in analogy with the "Phillips effect"[8] for which vertically homogeneous stirring leads to inhomogeneous mixing of the background buoyancy gradient, resulting in spontaneous layering of a stably stratified fluid. The Phillips effect has been extensively studied. It has also been clearly demonstrated experimentally by Ruddick *et al.*[9] The *PV-Phillips effect* makes a similar argument for positive-feedback resulting from inhomogeneous lateral mixing of PV along stratification surfaces. Formation and sharpening of jets is related to PV mixing via PV inversion. Moreover, Juckes and McIntyre[10] argue that straining of the turbulence by jet shear can considerably enhance the positive feedback. In this work, we show that a reduced model of two coupled mean fields exhibits both the formation of staircases in the mean density field, and a lattice of layers/jumps in the mean vorticity field. Reference 11 reported the observation of a quasi-periodic $E \times B$ flow pattern in the numerical results of gyrokinetic simulations. This was termed the "$E \times B$ staircase," inspired by the aforementioned planetary analogs. These staircases were spontaneously formed, and self-organizing, with a long lifespan. Moreover, T_i corrugations coincided with these flow shears. In-between the shear layers, regions of turbulent avalanching exist. Furthermore, Ref. 12 reported the experimental evidence for coherent shearing-turbulence modulational states in the Tore Supra tokamak. These results are consistent with interpretation as an $E \times B$ staircase, though much more data is required to make a conclusive identification. What is missing in both of these works is the explanation of what the underlying mechanism is by which these shear patterns and pressure corrugations spontaneously form and exist over long periods of time. Hence, computer simulations and experimental observations alone are not sufficient and the need for a reduced model is clear.

There have been extensive theoretical studies on the nonlinear growth rates of zonal shearing fields and their comparison to numerical simulations[13–16] of drift waves (DW) turbulence systems. Also, there have been some efforts

towards understanding the saturation mechanisms of zonal flows.[13,17,18] The trade off of energy between the zonal shearing fields and the turbulence populations have been studied using reduced predator-prey models.[19] The well established self-regulating "predator-prey" feedback loop nature of the DW-ZF system has been observed in numerous experiments[20,21] simulations.[22] This suggests that the models of staircase formation should continue in this vein.

However, the spatial structure of the zonal shearing fields and their evolution in time and space remain poorly understood. Understanding of the evolution of the mesoscale structure of the mean density and shearing fields in both time and space is the motivation and focus of this work. Here, we explore a theoretical model for the study of a simple DW-ZF flow turbulence system. By studying the spatial structure of the shearing field and the density profile, we aim to achieve a goal of a better understanding of two main subjects:

(1) The evolution and formation of quasiperiodic mesoscale density staircase structure, and the associated mesoscale shearing lattice pattern.
(2) Emergence of a steady state, macroscale transport barrier from the mesoscale density staircase, as a result of a global transport bifurcation. Note, the point here is that a mesoscale pattern condenses to form a macroscopic barrier. This is different from a direct transition on macroscales.

The basic physics model of DW-ZF flow turbulence was developed from fundamental ideas for 2D and quasi-geostrophic (QG) fluid dynamics. Hasegawa, Mima, and collaborators first emphasized the relevance of these ideas to drift wave system. We present a brief primer of the key ideas of these models below, in outline form.

– All of the 2D fluid QG and Hasegawa-Mima (HM) equations are statements of potential vorticity (PV) conservation along fluid trajectories. For HM model, $\mathrm{PV} \equiv q = \log n - \rho_s^2 \nabla^2 (e\phi/T)$.
– All of these systems support two inviscid quadratic invariants, energy and potential enstrophy (PE), where PE is defined as $U = \frac{1}{2} q^2$.
– Dual conservation forces a dual cascade, forward for potential enstrophy and inverse for energy. The inverse energy cascade generates flow structures on a large scale.
– The forward cascade (to small scale dissipation) of potential enstrophy implies that PV is mixed and coupled to small-scale dissipation.
– PV mixing and any inhomogeneity in the mean PV profile (i.e., a seed in the shear) imply that there will be a PV flux, or transport. One element of a PV flux is a vorticity flux, i.e., $\langle \tilde{v}_r \nabla^2 \tilde{\phi} \rangle \neq 0$. Here, the inhomogeneity is radial.
– A vorticity flux, and one direction of symmetry (toroidal, in a tokamak, azimuthal in 2D models) in turn imply a Reynolds Force (i.e., $\langle \tilde{v}_r \nabla^2 \tilde{\phi} \rangle = \partial_r \langle \tilde{v}_r \tilde{v}_\theta \rangle \neq 0$), and thus the ZF generation.

This reduced model is based upon the Hasegawa-Wakatani (HW) system of equations for DW turbulence.[23,24] The HW system is a simple 2D system describing the collisional drift wave instability driven turbulence which conserves the energy and PE. Furthermore, conservation of PE leads to the spontaneous generation of ZF by turbulence (Reynolds stress). Following the theoretical prediction of ZF generation by DW turbulence, turbulence-driven ZF was observed in nonlinear simulations of various fluid plasma turbulence models.[25–29]

Our system variables are functions of time and radius, and consist of the mean (reduced) density n (defined in Eq. (5)), the mean vorticity u, and the turbulent PE ε. In order to obtain the system of nonlinear equations, mean field expressions for the flux of particles and vorticity obtained for the HW system[30] are used. Furthermore, mixing length estimates are constructed to obtain the functional forms for the nonlinear, local diffusion coefficients. The prescription for the mixing length form (which is also employed in Refs. 31 and 32) is similar to the one presented in Ref. 33 by Balmforth *et al* for their model of buoyancy layering in a the stably stratified fluid, in that it is a nonlinear hybrid of two length scales; a constant forcing scale l_0 and a dynamic length scale which is a function of the system variable. In our system, this dynamic length scale is taken to be the Rhines scale l_{Rh} (defined in Eq. (38)), which is a function of ε and the mean potential vorticity gradient $(\partial_x q)$.[31,32] The choice of the functional form of l_{Rh} is essential for the positive feedback which drives the feature forming instabilities and leads to the formation of nonlinear density staircase and shearing lattice. PV is conserved along the fluid trajectories. Inhomogeneous mixing leads to a sequence of mixed layers and regions of profile steepening. Inhomogeneity is assured by the synergy of coherent modulation with gradient dependent feedback through l_{Rh}.

Numerical solutions of our reduced model show that the evolution of structures proceeds in roughly three stages. The structures develop from linear instabilities in small microscales. These are secondary modulational instabilities, in contrast to the primary linear DW instabilities. These features evolve to large amplitude, mesoscale structures by local reorganization and coalescence. At larger scales, coalescence stops and the structures detach from their position of formation and propagate towards the boundaries, until the evolution ends with the formation of a steady macroscale barrier. We should note that a pattern propagation was also advocated by Kosuga *et al.*,[34,35] in an alternative theory approach to $\mathrm{E} \times \mathrm{B}$ shear layer pattern formation due to the propagation of heat-flux modulations.

For the study of the global transport bifurcation of the steady macro-state, an external particle flux drive, Γ_0, is used for a control parameter. We observe that the steady macro-state of a system driven by an external particle flux undergoes a global transport bifurcation, from a normal confinement (NC) state to an enhanced confinement state (EC), as the amplitude of the flux drive increases beyond a threshold of transition Γ_{th}. The EC state is characterized by a flattened density profile in the inner region, while in the outer region, the density profile is steep, and the levels of turbulent PE and turbulent particle flux drop considerably, relative to the inner region. We also explore the globally averaged particle flux-density gradient landscape and observe the hysteresis behavior as Γ_0 is first increased and then decreased.

The rest of this paper is organized as follows: In Section II, the derivation of the nonlinear reduced model for 2D HW system is presented, which includes three nonlinear coupled evolution equation for the system variables, density, vorticity, and turbulent PE. In Section II A, the mixing length function is introduced and the physics of Rhines scale is discussed. In Section II B, the condition for linear instability of the simple equilibria for the reduced model is obtained, in search of the parameter ranges where the formation of nonlinear structures is possible. In Section III, detailed numerical results are presented for the solution of the reduced model equations. The structure formation is traced from microscale linear instabilities to the formation of mesoscale barriers, and finally the formation of macro barriers. In Section III B, the dependence of the solutions on some of the parameters is discussed, including turbulence spreading of PE, initial density gradient, and the collisional viscosity. In Section IV, an external particle flux drive is added to the density equation, and the mean profile structure emerging from this dynamics and the transport bifurcation of the steady state are studied. In Section IV A, the particle flux-density gradient landscape is explored, and in Section IV B, the physics of hysteresis in the global flux-gradient relation is analyzed. We summarize the findings and discuss the directions of our related future works in the discussion and conclusion, Section V.

II. THE MODEL

The model equations[23] which describe the electrostatic DW turbulence in a straight magnetic field are the vorticity equation

$$\frac{d}{dt}\left(\nabla^2\varphi\right) = \eta\nabla_\parallel^2(\log N - \varphi) + \mu_c\nabla_\perp^4\varphi, \tag{1}$$

and the continuity equation:

$$\frac{d}{dt}\log N = \eta\nabla_\parallel^2(\log N - \varphi) + D_c\nabla_\perp^2\log N. \tag{2}$$

Here N is the electron density, and $\varphi = e\phi/T_e$ is the non-dimensional electric potential, $\eta = T_e/m_e\nu_{ei}\rho_s c_s$ is the non-dimensional parallel diffusion coefficient, time is normalized to $1/\omega_{ci} = m_i c/eB$ (ω_{ci} is the ion cyclotron frequency), and the spatial dimensions are normalized to $\rho_s = (T_e/m_i)^{1/2}/\omega_{ci}$, the ion sound radius. The terms proportional to μ_u and D_c are respectively the collisional viscosity and diffusivity terms which remove energy from fine scales. The convective derivative is given by

$$\frac{d}{dt} = \frac{\partial}{\partial t} + \mathbf{v}_E.\nabla, \tag{3}$$

$$\mathbf{v}_E = \hat{z}\times\nabla\varphi. \tag{4}$$

Moreover, the notation is simplified by defining n, v, and u as

$$n \equiv \log(N/N_0), \quad \mathbf{v} \equiv \mathbf{v}_E, \quad u \equiv \nabla_\perp^2\varphi, \tag{5}$$

where n is the reduced density, and N_0 is a normalization constant. n, N, $\mathbf{v}$, and u are expanded in terms of a mean part and a perturbation part as

$$\begin{aligned} n &= \langle n\rangle + \delta n(x,y,z,t),\\ N &= \langle N\rangle + \delta N(x,y,z,t), \end{aligned} \tag{6}$$

where the averaging is over the directions of symmetry (z, y). With the assumption of small perturbations ($\epsilon = \delta N/\langle N\rangle \ll 1$), we obtain

$$\log N \approx \log\langle N\rangle + \frac{\delta N}{\langle N\rangle} - \frac{1}{2}\left(\frac{\delta N}{\langle N\rangle}\right)^2 + \cdots \tag{7}$$

Comparing Eqs. (7) and (6), we obtain

$$\langle n\rangle \approx \log\frac{\langle N\rangle}{N_0} + O(\epsilon^2), \tag{8}$$

$$\delta n \approx \frac{\delta N}{\langle N\rangle} + O(\epsilon^2). \tag{9}$$

Similar to Eq. (6), u and $\mathbf{v}$ are expanded to obtain

$$\begin{aligned} u &= \langle u\rangle + \delta u(x,y,z,t)\\ \mathbf{v} &= \langle \mathrm{v}\rangle\hat{y} + \delta\mathbf{v}(x,y,z,t), \end{aligned} \tag{10}$$

where $\langle u\rangle = \partial_x\langle \mathrm{v}\rangle$. Equations (1) and (2) are averaged over the directions of symmetry to obtain the time evolution equations for the mean density n and vorticity u

$$\partial_t\langle u\rangle + \partial_x\langle\delta v_x\delta u\rangle - \mu_c\nabla_\perp^2\langle u\rangle = 0, \tag{11}$$

$$\partial_t\langle n\rangle + \partial_x\langle\delta v_x\delta n\rangle - D_c\nabla_\perp^2\langle n\rangle = 0. \tag{12}$$

Subtracting Eqs. (11) and (12) from Eqs. (1) and (2), the fluctuation equations are obtained as

$$\begin{aligned} &(\partial_t + \langle \mathrm{v}\rangle\partial_y)\delta n + \{\delta\varphi,\delta n\} + \delta v_x\partial_x\langle n\rangle - \mu_c\nabla_\perp^2\delta n\\ &\quad = \eta\nabla_\parallel^2(\delta n - \delta\varphi), \end{aligned} \tag{13}$$

$$\begin{aligned} &(\partial_t + \langle \mathrm{v}\rangle\partial_y)\delta u + \{\delta\varphi,\delta u\} + \delta v_x\partial_x^2\langle \mathrm{v}\rangle - D_c\nabla_\perp^2\delta u\\ &\quad = \eta\nabla_\parallel^2(\delta n - \delta\varphi). \end{aligned} \tag{14}$$

The set of Eqs. (13) and (14) are the nonlinear HW equations in the presence of the flow and flow shear as an additional source of free energy. These equations locally conserve the potential vorticity (PV) which is defined as $q = n - u$, up to the collisional dissipation terms. PV mixing and transport has been shown to be fundamental to the formation of zonal flows.[4] PV is similarly described in terms of a mean and fluctuation term

$$q = \langle q\rangle + \delta q(x,y,z,t). \tag{15}$$

We subtract Eq. (13) from Eq. (14) to obtain the evolution equation for $\delta q = \delta n - \delta u$

$$(\partial_t + \langle \mathrm{v}\rangle\partial_y)\delta q + \{\delta\varphi,\delta q\} + \delta v_x\partial_x\langle q\rangle - \mu\nabla_\perp^2\delta q = 0, \tag{16}$$

where only the viscous dissipation is kept as the dominant turbulence dissipation mechanism. Multiplying the above

equation by δq and averaging over the directions of symmetry yields

$$\partial_t\langle\delta q^2\rangle + \partial_x\langle\delta v_x\delta q^2\rangle = -\langle\delta v_x\delta q\rangle\partial_x\langle q\rangle - \mu_\varepsilon\langle|\nabla_\perp\delta q|^2\rangle + P, \tag{17}$$

where $\mu_\varepsilon \approx (\mu_c + k_\perp^2 D_c)/(1+k_\perp^2)$ is the effective collisional diffusion of the turbulent PE. The above equation describes the time evolution of the turbulent potential enstrophy

$$\varepsilon = \langle\delta q^2\rangle/2. \tag{18}$$

The second term is the nonlinear spreading of the turbulent PE flux. The third term is the internal turbulence production mechanism which converts the mean PE into turbulent PE (and vice versa). This production term conserves the total PE of the system. The fourth term is the turbulence dissipation term resulting from the forward cascade of turbulent PE toward the small dissipation scale. The last term P is an external source of turbulence production. Following Ref. 30, the quasilinear expression for turbulent PV flux $\Gamma_q = \langle\delta v_x\delta q\rangle$ is

$$\langle\delta v_x\delta q\rangle = -\chi\partial_x\langle q\rangle, \tag{19}$$

$$\chi = \sum_{\mathbf{m}} \frac{\gamma_{\mathbf{m}}}{|\langle\mathrm{v}\rangle - \omega_{\mathbf{m}}/k_m|^2}\langle\delta\varphi_{\mathbf{m}}^2\rangle, \quad \mathbf{m} = (m,n,l), \tag{20}$$

where in Eq. (20), the summation is over all the azimuthal m, parallel n, and radial l drift mode numbers, $\gamma_{\mathbf{m}}$ is the mode growth rate, $\omega_{\mathbf{m}}$ is the mode eigenfrequency, and k_m is the azimuthal wave number. In the near-adiabatic regime, for which the parallel diffusion rate $\eta k_\parallel^2$ is the dominant rate (i.e., $\eta k_\parallel^2 \gg \omega_m, k_m\langle\mathrm{v}\rangle$), DW frequency is given by

$$\omega_{\mathbf{m}} = \frac{k_m v_d(x)}{1+k_\perp^2}, \tag{21}$$

$$v_d(x) = -\partial_x\langle n\rangle, \tag{22}$$

where $k_\perp^2 = k_r^2 + k_m^2 = -(\nabla_\perp^2\delta\varphi)/\delta\varphi$, and $k_\perp$ is the perpendicular mode number. In Eq. (21), the DW frequency is proportional to the *local* density gradient. Hence, the quasilinear expression for turbulent particle flux $\Gamma = \langle\delta v_x\delta n\rangle$, is given by[30]

$$\Gamma = -D_n\partial_x\langle n\rangle + V_{\mathrm{pinch}}, \tag{23}$$

$$D_n(x) = \sum_{\mathbf{m}} \frac{k_\perp^2}{1+k_\perp^2}\frac{k_m^2}{\eta k_\parallel^2}\langle\delta\varphi_{\mathbf{m}}^2\rangle, \tag{24}$$

$$V_{\mathrm{pinch}}(x) = \langle\mathrm{v}\rangle\left(\sum_{\mathbf{m}} \frac{k_m^2}{\eta k_\parallel^2}\langle\delta\varphi_{\mathbf{m}}^2\rangle\right). \tag{25}$$

In deriving Eqs. (23) and (24), the modes are taken to be *local* drift waves (DW). In our future work, we will investigate the *global* modes, for which the eigenfrequencies and growth rates are constant in radius. These global modes are pertinent to magnetic shear-free devices, such as linear machines, for which the width of the modes span the whole plasma radius. We add that in tokamaks with approximately flat safety factor (q) profile, due to the weak magnetic shear modes that can spread over the flat-q region. The convective pinch term defined in Eq. (25) results from the mean $E\times B$ flow velocity. The turbulent vorticity flux $\Pi = \langle\delta v_x\delta u\rangle$ is given by[30]

$$\Pi = (\chi - D_n)\partial_x\langle n\rangle - \chi\partial_x^2\langle\mathrm{v}\rangle, \tag{26}$$

where χ and D_n are respectively given by Eqs. (20) and (24). The first term on the right-hand-side (RHS) of Eq. (26) is the residual vorticity. Through this term, the free energy of density gradient can be converted into positive Reynolds work, resulting in the generation of flow shear. The second term on the RHS is the turbulent viscous diffusion, which is responsible for relaxing the vorticity gradient through dissipation. The quasilinear expressions in Eqs. (19), (23), and (26) are used to build the reduced turbulence model.

Based on these arguments, the set of reduced evolution equations describing the system is given by

$$\partial_t n = \partial_x D_n\partial_x n + D_c\partial_x^2 n, \tag{27}$$

$$\partial_t u = \partial_x(D_n - \chi)\partial_x n + \chi\partial_x^2 u + \mu_c\partial_x^2 u, \tag{28}$$

$$\partial_t\varepsilon = \partial_x D_\varepsilon\partial_x\varepsilon + \chi[\partial_x(n-u)]^2 - \varepsilon_c^{-1/2}\varepsilon^{3/2} + P, \tag{29}$$

where in Eqs. (27)–(29), $\langle\ \ \rangle$ has been dropped to simplify the notation. Thus, from here forward n, u, and ε respectively represent the mean density, vorticity, and fluctuation PE. In Eq. (29) the term $-\varepsilon_c^{-1/2}\varepsilon^{3/2}$ is the dissipative term, resulting from the forward cascade of PE (enstrophy dissipation rate is $(\varepsilon/\varepsilon_c)^{1/2}$, and ε_c is a non-dimensional parameter). The particle pinch term V_{pinch} is assumed to be negligible compared to the diffusive terms and is not included in Eq. (27). Effects of V_{pinch} will be studied in future works. Furthermore, Fickian diffusive flux form is used for the turbulent flux of PE: $\langle\delta v_x\varepsilon\rangle = -D_\varepsilon\partial_x\varepsilon$, where D_ε is the turbulent PE diffusion coefficient. The external turbulence production source in Eq. (29), i.e., P, is due to sources of free energy which are external to the closed system described by Eqs. (1) and (2). The production term due to this mechanism has the form $P = \gamma_\varepsilon\varepsilon$; it is linear in ε and is proportional to γ_ε, the characteristic growth of the instabilities responsible for P. Alternatively, one can adopt the mechanism of stirring as the method for driving the turbulence in the system. Stirring creates wakes at a rate given by U. Turbulence will break down these wakes on a timescale given by the eddy turnover rate $\varepsilon^{-1/2}$. As a result, the stirring production term is given by $P = U^2\varepsilon^{1/2}$. Adopting either form for P gives similar results; thus we use the former mechanism as the external production term.

Imposing the condition $\partial_x\varepsilon = 0$ at the boundaries prevents the influx-outflux of turbulent PE. As a result, the system described by the set of Eqs. (27)–(29), manifestly conserves the total PE (sum of mean and turbulent PE), up to damping terms and external forcing. We show this as follows: we subtract Eq. (28) from Eq. (27), multiply the result by $n-u$, add the result with Eq. (29), and integrate over x to obtain

$$\partial_t E = \int_0^L \left(\partial_t \frac{(n-u)^2}{2} + \partial_t \varepsilon \right) dx$$
$$= \int_0^L \Big(P - \varepsilon_c^{-1} \varepsilon^{3/2} + [D_c + \mu_c] \partial_x n \partial_x u$$
$$- \mu_c (\partial_x u)^2 - D_c (\partial_x n)^2 \Big) dx. \quad (30)$$

In obtaining Eq. (30), the internal turbulence PE production term (second term on the RHS of Eq. (29)) is cancelled by the corresponding loss term in the evolution equation for the mean PE.

Mixing the length and phenomenological arguments are used to obtain the functional form of the turbulent diffusion coefficients D_n, χ and D_ε in Eqs. (11), (12), and (17). Using the quasilinear flux relations Eqs. (20) and (24), and in the near-adiabatic timescale ordering $\eta k_\parallel^2 \gg \omega_m \gg k_m \mathrm{v}$, D_n and χ are obtained ($\eta k_\parallel^2$ is the parallel resistive diffusion rate). For D_n, the approximation $|k_m \delta\varphi| = |\delta v_x| \approx l\varepsilon^{1/2}$ gives

$$D_n \approx \frac{k_\perp^2}{1+k_\perp^2} \frac{k_m^2 |\delta\varphi|^2}{\eta k_\parallel^2} \cong l^2 \frac{\varepsilon}{\alpha}, \quad (31)$$

where the parameter α is defined as the measure of the resistive diffusion rate in the parallel direction: $\alpha = \frac{1+k_\perp^2}{k_\perp^2} \eta k_\parallel^2$. From Eq. (20) for χ we can see that (unlike Eq. (24) for D_n) the denominator of the argument of the sum is not dominated by the large parallel diffusion rate $\eta k_\parallel^2$; rather it is a competition between the wave frequency ω and the flow shear. We obtain the functional form of χ in the limit of no flow-shear and then modify it to include the effect of flow shear. In the absence of flow shear, instabilities are collisional drift waves driven by the free energy of the density gradient. Therefore γ_m is given primarily by that of DWs, and is reduced by a viscous damping rate

$$\gamma_m = \gamma_{DW} - \gamma_\mu = c_\chi \frac{\omega_m^2}{\alpha}, \quad \gamma_{DW} = \frac{k_\perp^2}{1+k_\perp^2} \frac{\omega_m^2}{\eta k_\parallel^2}, \quad (32)$$

where γ_{DW} is the DW growth rate in the near adiabatic regime ($\eta k_\parallel^2 \gg \omega_m$), and $-\gamma_\mu$ is the viscous damping rate of the mode and $c_\chi = 1 - \gamma_\mu / \gamma_{DW}$. From Eq. (20), we obtain

$$\chi(x) = \sum_{\mathbf{m}} \frac{\gamma_{\mathbf{m}}}{|\langle \mathbf{v} \rangle - \omega_{\mathbf{m}}/k_m|^2} \langle \delta\varphi_{\mathbf{m}}^2 \rangle$$
$$\approx \frac{c_\chi \frac{\omega_m^2}{\alpha}}{\omega_m^2} |k_m \delta\varphi|^2 \approx c_\chi l^2 \frac{\varepsilon}{\alpha}. \quad (33)$$

The strength of turbulent viscosity (χ) involves the constant-multiplier c_χ. In obtaining Eq. (33), we used Eq. (32) for $\gamma_{\mathbf{m}}$ and the approximations $|k_m \delta\varphi| = |\delta v_x| \approx l\varepsilon^{1/2}$ and $\langle \mathbf{v} \rangle \ll \omega_{\mathbf{m}}/k_m$. Furthermore, the effect of strong flow shears is incorporated into χ using the following prescription:

$$\chi(x) \cong c_\chi l^2 \frac{\varepsilon}{\sqrt{\alpha^2 + a_u u^2}}. \quad (34)$$

Finally, the following form is employed to approximate the scattering of turbulence intensity D_ε:

$$D_\varepsilon(x) \cong \beta l^2 \varepsilon^{1/2}. \quad (35)$$

The form of D_ε is chosen based on dimensional arguments (l for spatial variation and $\varepsilon^{-1/2}$ for time variation), and the parameter β is adjustable so as to explore the effect of turbulence spreading of PE by varying it.

A. The mixing length

The Rhines scale is an emergent intensity dependent scale in DW - quasi-geostrophic turbulence. The Rhines scale l_{Rh} is defined by the crossing of eddy turnover rate and the three-wave mismatch frequency for drift waves $\omega_{MM} \sim \omega$. At $l \sim l_{Rh}$, the DW frequency is approximately given by

$$\omega \approx -\frac{k_x \partial_x n}{1+k_\perp^2} \approx l_{Rh} |\partial_x q|, \quad (36)$$

where the simplifying assumption $k_\perp^2 > 1$ has been made. Eddy turnover rate can be approximated as

$$1/\tau_c = \frac{\delta v}{l_{Rh}} \sim \varepsilon^{1/2}. \quad (37)$$

Equating the wave time-scales Eq. (36) to eddy time-scale Eq. (37) we obtain the Rhines scale as

$$l_{Rh} = \frac{\sqrt{\varepsilon}}{|\partial_x q|}. \quad (38)$$

For $l < l_{Rh}$, the turbulence is eddy-like and the inverse cascade occurs. For $l > l_{Rh}$ the turbulence is weak and wave-like and co-exists with the ZF (as resonant interaction occurs by DW-ZF coupling). Nonlinear coupling is weaker for $l > l_{Rh}$. As $l_{Rh} \sim (\partial_x q)^{-1}$, steeper gradients will drive l_{Rh} smaller, ensuring weaker mixing for a larger band of scales. This creates the required feedback loop, which weakens the transport as gradients steepen. Note this follows from the basic structure of the wave dispersion and mode coupling.

It is useful to contrast the Rhines scale and the standard mixing length theory. In the mixing length theory (as practiced in fusion transport modeling), one takes eddy turnover rate of order wave frequency and estimates the level of turbulence $\delta n/n \sim k_\perp L_n$. In the Rhines model, one uses the known turbulence level and estimates the scale for crossover implied by that level. It is evident that these two models are really equivalent.

In this model, inhomogeneous mixing of PV results from the dynamic mixing length, l. We employ the following model for the mixing length

$$l = \frac{l_0}{\left(1 + l_0^2 [\partial_x (n-u)]^2 / \varepsilon\right)^{\kappa/2}}. \quad (39)$$

In the above equation, l_0 is the length-scale related to the turbulent forcing mechanism and the other significant length-scale in the system is the Rhines scale, ($l_{Rh} = \sqrt{\varepsilon}/|\partial_x q|$). In a system with weak mean PV gradient such that $l_0 < l_{Rh}$, l_0 is the natural choice for the length-scale of turbulent mixing. In quasi-2D HW system, energy inverse-cascades from the

forcing scale l_0 to larger length scales, while enstrophy forward cascades from l_0 to the small dissipation scale l_d. Eddies in the inverse energy cascade spectral range (i.e., $l < l_0$) grow in size, become slower and more wave-like, and gradually transform into drift waves at the Rhines scale. In the limit where the PV gradient is weak (i.e., l_{Rh}^{κ} is larger than l_0) the mixing length is given by the forcing length scale l_0. However, locally the PV gradient of the system can become strong enough such that $l_{Rh} < l_0$ and the mixing length can be approximated by $l \sim l_0^{1-\kappa} l_{Rh}^{\kappa}$. At these locations of steep PV gradient, l_{Rh} is the governing spatial scale for the turbulence.

The choice of mixing length given by Eq. (39) is a crucial element of this model. It acts to close the feedback on PV gradient steepening by reducing the turbulent diffusivity, and turbulence intensity (represented by ε). The feedback loop develops from steepening in the mean PV gradient, which is followed by the drop in local turbulent PE, i.e., ε, due to PE conservation. With the choice of Eq. (39) for the mixing length, rise in $\partial_x q$ and drop in ε further result in the drop of l and of turbulent PV, i.e., Γ_q. This in turn further contributes to the steepening of the mean PV, and this closes the feedback loop.

Instabilities driven by this feedback loop mechanism result from a local transport bifurcation. Manifestation of the transport bifurcation in the turbulent flux versus the mean gradient relation is the formation of an *S-curve*, similar to the solid curve in Fig. 1. The *S-curve* consists of two stable mean gradient ranges at which $\delta\Gamma_q/\delta|\nabla q| > 0$, enclosing the region of negative diffusion at which $\delta\Gamma_q/\delta|\nabla q| < 0$. The positive feedback loop in the negative diffusion region drives the instabilities which lead to nonlinear feature formation in the mean profile.

We reduce the number of parameters in the system by the following rescaling choices:

$$\hat{x} = x/L, \quad \hat{t} = \gamma_\varepsilon t (l_0/L)^2, \quad \hat{\varepsilon} = \varepsilon/\gamma_\varepsilon^2, \\ \hat{n} = n\frac{l_0}{L\gamma_\varepsilon}, \quad \hat{u} = u\frac{l_0}{L\gamma_\varepsilon}, \tag{40}$$

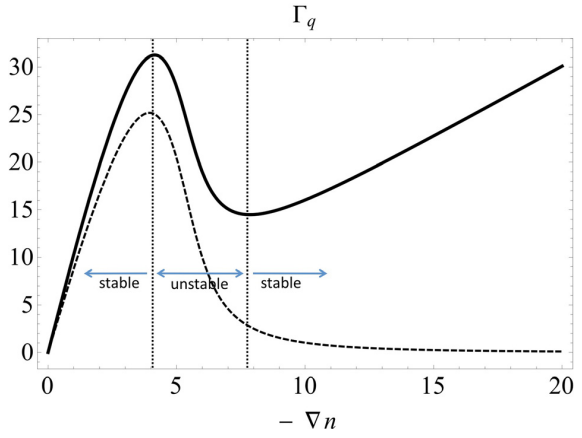

FIG. 1. Plot of the flux of PV versus the density gradient for the calculated equilibrium values obtained for $\alpha = 10$, $\varepsilon_0 = 9$, and $\mu_c = 1.5$. The dashed curve is only the turbulent PV flux and the solid curve includes the collisional diffusion ($\propto \mu_c$), which results in the second positive slope branch of the curve.

$$\hat{l} = l/l_0, \quad \hat{\alpha} = \alpha/\gamma_\varepsilon, \quad \hat{\mu}_c = \mu_c/(\gamma_\varepsilon l_0^2), \quad \hat{a}_u = a_u (L/l_0)^2. \tag{41}$$

As a result, the rescaled set of evolution equations is given by

$$\partial_t n = \partial_x \left[\left(\frac{l^2 \varepsilon}{\alpha} \right) \partial_x n \right] + D_c \partial_x^2 n, \tag{42}$$

$$\partial_t u = \partial_x \left[\left(\frac{l^2 \varepsilon}{\alpha} - \frac{c_\chi l^2 \varepsilon}{\sqrt{\alpha^2 + a_u u^2}} \right) \partial_x n \right] \\ + \frac{c_\chi l^2 \varepsilon}{\sqrt{\alpha^2 + a_u u^2}} \partial_x^2 u + \mu_c \partial_x^2 u, \tag{43}$$

$$\partial_t \varepsilon = \beta \partial_x \left[l^2 \varepsilon^{1/2} \partial_x \varepsilon \right] \\ + \Lambda \left[\frac{c_\chi l^2 \varepsilon}{\sqrt{\alpha^2 + a_u u^2}} \left[\partial_x (n-u) \right]^2 - \frac{\varepsilon^{3/2}}{\varepsilon_c^{1/2}} + \varepsilon \right], \tag{44}$$

where we have defined $\Lambda = L^2/l_0^2$ and dropped the hat symbols to simplify our notation. The rescaled nondimensional form of l is given by

$$l = \frac{1}{\left(1 + \left[\partial_x (n-u) \right]^2 / \varepsilon \right)^{\kappa/2}}. \tag{45}$$

B. Equilibria and their stability

Here we look for the parameter ranges in which the equilibria are unstable, and there is possibility for the growth and formation of structures in density and vorticity profiles. We consider the equilibrium solutions for which the system has a uniform density gradient, uniform turbulent PE, and no flow shear

$$\partial_x n = -g_0, \quad u = 0, \quad \varepsilon = \varepsilon_0. \tag{46}$$

For these equilibrium conditions from Eq. (44) and for a steady solution of the PE density equation, we have

$$\frac{c_\chi}{\alpha \left(1 + g_0^2/\varepsilon_0 \right)^{\kappa}} g_0^2 - \frac{\varepsilon^{1/2}}{\varepsilon_0^{1/2}} + 1 = 0. \tag{47}$$

The above equation expresses the balance between the production terms and the dissipation term in the steady state. From Eq. (47), for a given g_0, ε_0 can be obtained. Flux of PV for these equilibrium values, and for the simple case of $\mu_c = D_c$ is given by

$$\Gamma_q(g_0) = \Gamma_n - \Gamma_u = \frac{c_\chi \varepsilon_0}{\alpha \left(1 + g_0^2/\varepsilon_0 \right)^{\kappa}} g_0 + \mu_c g_0, \tag{48}$$

where Γ_q is a function of the single parameter g_0. In the Appendix, we show that the linear perturbations are unstable if

$$\frac{\delta \Gamma_q}{\delta g_0} < 0. \tag{49}$$

The above condition expresses the *negative diffusion* of PV. In Fig. 1, we have plotted Γ_q versus g_0 using the relation

given for Γ_q in Eq. (48) for the values $\alpha = 10$, $\varepsilon_0 = 9$, and $D_c = \mu_c = 1.5$. The dashed curve is only the turbulent part of PV flux ($\Gamma_q - \mu_c g_0$) and the solid curve (known in the literature as the "S-curve") includes the collisional diffusion ($\propto \mu_c$), which results in the second positive slope branch of the curve. From Fig. 1, we can see that for the range of values of $4.5 < g_0 < 7.5$, the condition given by Eq. (49) is satisfied, and as a result, the equilibria within this parameter range are unstable.

III. NUMERICAL SOLUTIONS OF THE REDUCED MODEL

In this section, the numerical solutions of the nonlinear Eqs. (42), (43), and (44) are explored. A finite difference method in space is used, and the time integration is performed using the Runge-Kutta-Fehlberg method. Initial conditions are chosen as

$$n(x, t = 0) = -g_i x; \quad u(x, t = 0) = 0; \quad \varepsilon(x, t = 0) = \varepsilon_i. \tag{50}$$

The values g_i, ε_i are taken from the region in parameter space which is linearly unstable. The boundary conditions are as follows:

$$n(0, t) = 0, \quad n(1, t) = -g_i, \tag{51}$$

$$u(0, t) = u(1, t) = 0. \tag{52}$$

With the above boundary condition (BC) for density, the value of n is maintained at a constant value through fluxes of density at the boundaries ($\partial_x n(x = 0, 1; t) \neq 0$). Moreover, Eq. (52) sets the radial flux of azimuthal momentum at the boundaries to zero (since $u = \partial_x \mathrm{v}$). For the turbulent PE equation, both choices of BC are explored

$$\varepsilon(0, t) = \varepsilon(1, t) = \varepsilon_i, \tag{53}$$

$$\partial_x \varepsilon(0, t) = \partial_x \varepsilon(1, t) = 0. \tag{54}$$

In Section IV, the value of the density at $x = 0$ is allowed to evolve due to an external particle source (written as the divergence of an imposed particle source) sharply peaked at $x = 0$.

A. Formation and evolution of density staircase and vorticity corrugation

Numerical solutions of the system exhibit roughly three stages of evolution (1) development of nonlinear mesoscale features from microscale instabilities (2) evolution of mesoscale structure through local merger processes leading to the formation of mesoscale barriers (3) detachment of the structures from their conception locations and their migration towards the boundaries resulting in the formation of the steady macroscale structure. Each stage of evolution has a characteristic time-scale and length-scale.

In the first stage, features develop in the profiles due to the linear instability of the initial profiles. Growth of these instabilities results in the formation of nonlinear features in the mean profiles, as well as in the turbulent PE profile. In the density profile, these features are in the form of staircases; i.e., series of jumps (steepening) and steps (flattening) in the density profile. Simultaneously, the vorticity profile develops the jagged (corrugated) features. These developed features have a quasi-periodic pattern with a characteristic length scale l_q.

Figure 2 shows the density gradient profile shown at the early stages of evolution, up to $t = 0.2$, for the following set of parameters: $\Lambda = 4000, c_\chi = 0.95, \alpha = 6, \varepsilon_c = 6.25, \beta = 0.1, \mu_c = 0.78$, and for the initial values $g_i = 5.1, \varepsilon_i = 0.002$, and with Dirichlet BCs for PE ($\varepsilon(x = 0, 1; t) = 0$). For the choice of Dirichlet BCs for PE, feature formation starts at the boundaries and spreads to the inner region. The peaks

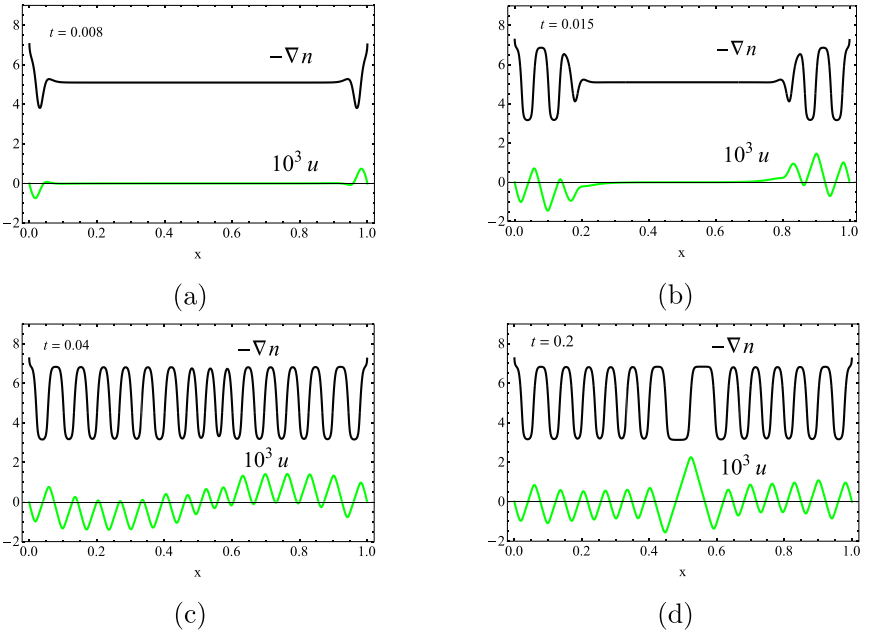

FIG. 2. Snapshots of density and vorticity profiles at times (2(a)) $t = 8 \times 10^{-3}$, (2(b)) $t = 1.5 \times 10^{-2}$, (2(c)) $t = 4 \times 10^{-2}$, and (2(d)) $t = 0.2$, showing the formation of steps from the boundaries towards the center of plasma for $\Lambda = 4000$, $c_\chi = 0.95$, $\alpha = 6$, $\varepsilon_c = 6.25$, $\beta = 0.1$, $\mu_c = 0.78$. Initial values are $g_i = 5.1$, $\varepsilon_i = 0.002$, and with Dirichlet BCs for PE ($\varepsilon(x = 0, 1; t) = 0$).

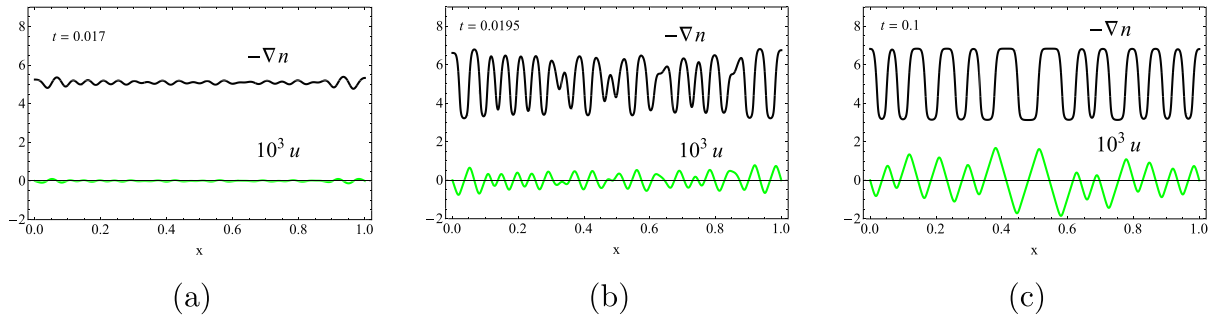

FIG. 3. Snapshots of density and vorticity profiles at times (3(a)) $t = 1.7 \times 10^{-2}$, (3(b)) $t = 1.95 \times 10^{-2}$, and (3(c)) $t = 0.1$, showing the global formation of steps in density profile and shear layers for the same parameters of Fig. 2, and with Neumann BCs for PE ($\partial_x \varepsilon(x = 0, 1; t) = 0$).

correspond to *jumps* in the density profile, and the troughs correspond to *steps*, or local flattenings, of the density profile. Moreover, between the times $t = 0.04$ and $t = 0.2$, two of the peaks in the range $0.5 < x < 0.6$ dissolve into neighboring peaks. Formation of steps in the density profile is accompanied by the formation of corrugations in the vorticity profile (u). Figure 2 also shows the formation of vorticity profile structures. Similar to the density profile, feature formation in the vorticity profile also starts at the boundaries and spreads to the inner regions.

However, for the choice of Neumann BCs for PE ($\partial_x \varepsilon(x = 0, 1; t) = 0$), feature formation in profiles is different from that observed previously, in that the initial instability grows almost at a uniform amplitude all along the radius. An example for a solution with Neumann BCs for PE is depicted in Fig. 3. These snapshots in time show that the features form uniformly along the radius, in contrast to Fig. 2(a) where the feature formation started at the boundaries and propagated towards the center.

The mean profiles evolve and transform through the process of local mergers. Merger between two jumps is shown in Fig. 4(a), and the merger between two steps is shown in Fig. 4(b). In Fig. 4(a), from the time $t = 0.55$, the trough at $x \approx 0.75$ gradually rises and dissolves before $t \approx 0.65$. In Fig. 4(b), from $t = 0.9$, the peak at $x \approx 0.65$ gradually falls and dissolves before $t \approx 1.05$. Dissolution of a peak is a merger between two steps (in the n profile), and the dissolution of a trough is a merger between two jumps (in the n profile). Merger of two jumps (steps) results in a wider jump (step).

Figure 5 shows the dynamics of vorticity profile, while the process of merger shown in Fig. 4 occurs in the density profile. The locations of the jumps (steps) in n coincide with locations of maximum negative (positive) slope in u. Moreover, merger results in increase in the amplitude of the resulting shearing layer in the vorticity profile.

Formation of steps in the density profile is accompanied by the formation of features in turbulent PE profile ε. Figure 6 compares the ∇n profile with the ε profile at the time $t = 0.2$. The level of ε is reduced at the spatial locations of jump in the density profile (peaks of $-\nabla n$). The PE profile in Fig. 6 forms from a small and uniform initial value of $\varepsilon_i = 0.002$. The value of ε quickly reaches the level comparable to Fig. 6. This level is the equilibrium solution value set by the initial value of the density gradient g_i. As a result, the solutions are not sensitive to the initial value of ε, so g_i is the control parameter of the system which determines the evolution of the solutions.

The process of mesoscale mergers gradually slows down and stops. Although beyond this evolutionary time, and away from the boundaries, the profiles formed are locally stationary, they will still evolve globally through spatial migration. Density staircase and the shear lattice detach from their positions of formation and migrate towards the boundaries. Migrating density barriers and shear layers

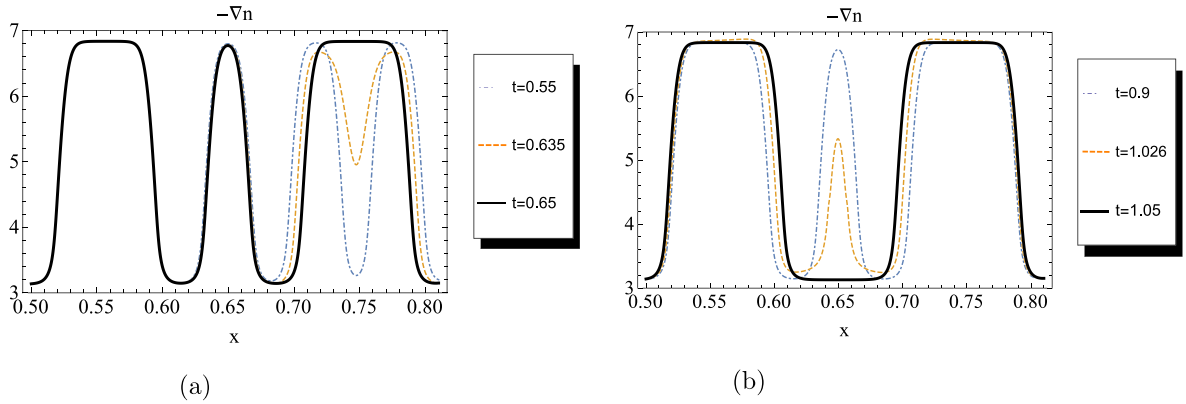

FIG. 4. Snapshots of the density profile ($0.5 < x < 0.8$) at times (a) $t = 0.55$ (blue), $t = 0.635$ (orange), and $t = 0.65$ (black), showing the merger between two jumps; and (b) $t = 0.9$ (blue), $t = 1.026$ (orange), and $t = 1.05$ (black) showing the merger between two steps.

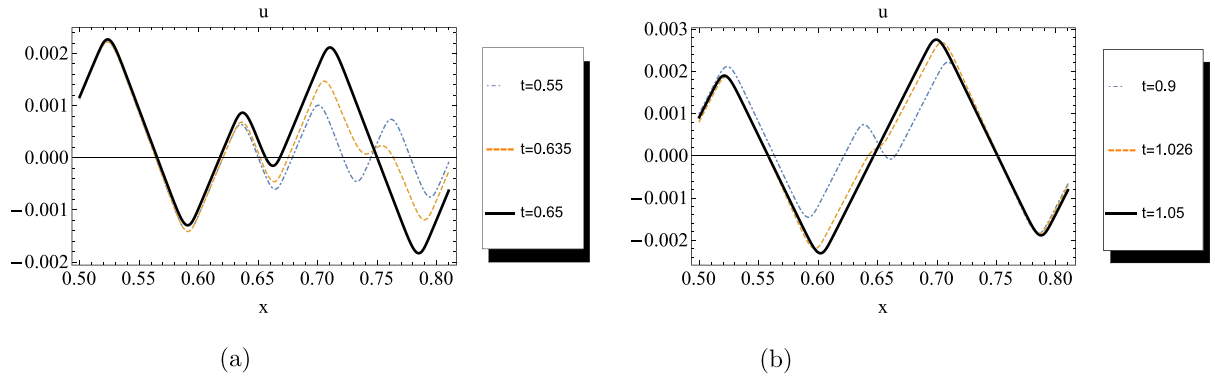

FIG. 5. Snapshots of the vorticity profiles for the same solution as Fig. 4, at times (a) $t = 0.55$ (blue), $t = 0.635$ (orange), and $t = 0.65$ (black); and (a) $t = 0.9$ (blue), $t = 1.026$ (orange), and $t = 1.05$ (black).

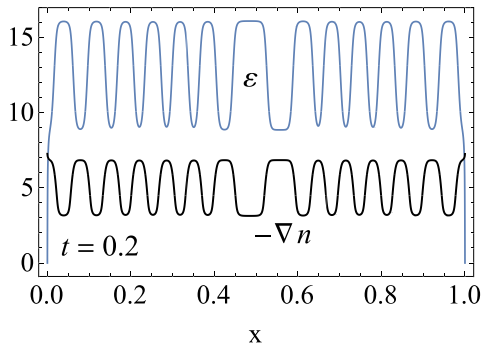

FIG. 6. Reduction in turbulence PE at the location of jumps in the density profile for the same parameters of Fig. 2.

condense as they reach the boundaries. This process continues until the steady, macroscale density barrier and the macroscale shearing profile form. Figure 7 shows the density and shearing profile during the migration stage. In Fig. 7(a), the density barriers move up the density gradient in an "escalator-like" motion. Moreover, Fig. 7(b) shows that along with the density profile, the shearing pattern moves in the same direction (i.e., to the left) and condenses at the boundary. The profile migration process takes place over a much longer evolutionary time $\sim O(10^4)$, in comparison to the earlier stages of evolution $\sim O(10^2)$ (note that time is scaled to $\gamma_\varepsilon^{-1}(L/l_0)^2$, where γ_ε is the external production). Therefore, most of the lifetime of the mesoscale features is spent migrating.

Evolution of density profile from the initial to the final macrostate is shown in a contour plot in Fig. 8. Different evolutionary stages are: (a) Formation of nonlinear features from linear instabilities and fast merger of micro-steps into meso-steps. (b) Coalescence of meso-steps into barriers. (c) Propagation of barriers along the gradient, and condensation at boundaries. (d) The stationary profile. At the same time, the vorticity (or shearing) profile evolves from the initial state for $u = 0$. Figure shows the evolutionary landscape of the vorticity profile u, as a function of position x and time t, for the same simulation run as Fig. 8. Evolution of the vorticity profile undergoes the identical stages: from micro to meso to the stationary macro profile (Fig. 9).

B. Parameter variation

The set of system equations depends on a large number of parameters. Here, we discuss the dependence of the numerical results on some of the parameters in the system namely, the PE turbulence spreading multiplier β, the initial density gradient g_0, and the collisional viscosity μ_c. Turbulence spreading is necessary for regulating the steepening in the PE turbulence profiles, and its absence will result in extreme sharpness in the gradients rendering the numerical solutions extremely stiff and practically unsolvable. Moreover, we find that the initial PV gradient to be the control parameter determining the outcome of the solutions and initial ε has little effect on the solutions. In our case, this is because we choose the initial system to be shear free, i.e., $u(t = 0) = 0$, so the initial PV is identical to the initial density

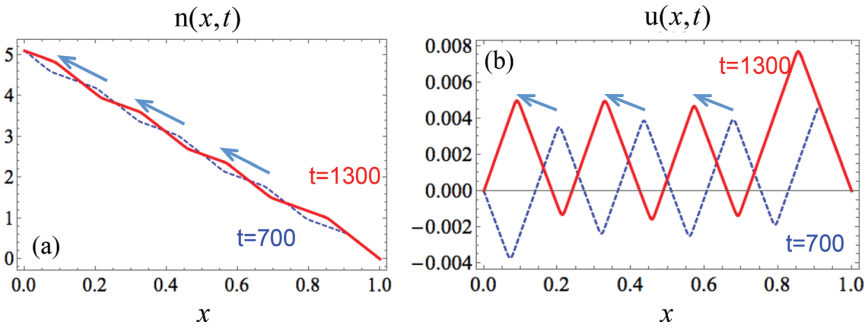

FIG. 7. (a) Upward, escalator-like migration of the step at times $t = 700$ and $t = 1300$. (b) Detachment of shearing pattern from the location of formation, and migration towards the boundary. Reprinted with permission from Ashourvan and Diamond, Phys. Rev. E **94**, 051202(R) (2016). Copyright 2016 American Physical Society.[36]

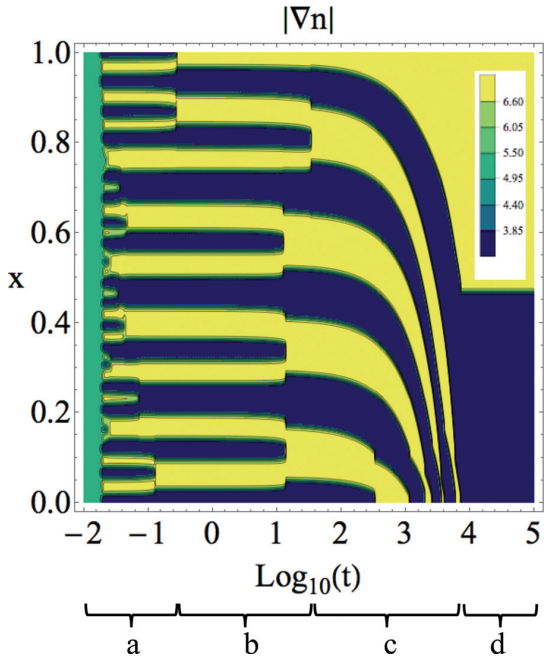

FIG. 8. Contour plot of the time evolution of $|\nabla n|$ along the plasma radius, for the same parameters as Fig. 2. Horizontal axis is the log of time, and the vertical axis shows the scaled radial location. Different stages of evolution are: (a) Fast merger of micro-steps and formation of meso-steps. (b) Coalescence of meso-steps to barriers. (c) Barriers propagate along the gradient, condense at boundaries. (d) Stationary profile. Reprinted with permission from Ashourvan and Diamond, Phys. Rev. E **94**, 051202(R) (2016). Copyright 2016 American Physical Society.[36]

gradient. Furthermore, since in most of the relevant realistic physical examples, the Prandtl number $Pr = \mu_c/D_c$ is large, μ_c is the more interesting physical damping parameter.

As the system variables evolve from their initial value, ε quickly reaches its equilibrium value set by the initial density gradient through Eq. (47). As a result, the numerical solutions are not sensitive to ε_i. However, the initial value of

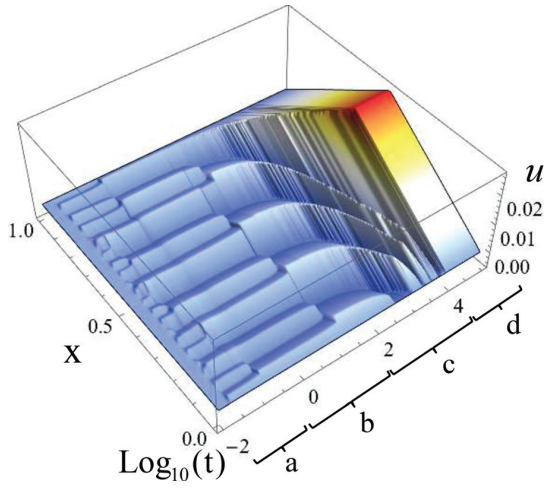

FIG. 9. Evolutionary landscape of the vorticity profile u (i.e., the shearing profile), as a function of position x and time t, for the same simulation run as Fig. 8. Reprinted with permission from Ashourvan and Diamond, Phys. Rev. E **94**, 051202(R) (2016). Copyright 2016 American Physical Society.[36]

the density gradient g_i is a control parameter that determines the evolution of the solutions. The maximum number of jumps formed during a simulation run can be controlled via g_i. Figure 10 shows the number of jumps formed at an early stage of evolution ($t = 0.1$). As g_i is raised, two jumps form at $g_i = 4.2$. Increasing the value of the initial density gradient from $g_i = 4.2$ to $g_i = 5.1$ results in the formation of larger number of jumps. Further increasing the density gradient from $g_i = 5.1$ to 5.7 will reduce the number of jumps formed. Beyond $g_i = 5.7$, no jumps or steps form in the system.

The width of the jump regions and step region which build the shape of the patterns is also sensitive to the initial value of the density gradient g_i. With increasing the initial value of the mean density gradient, the width of jumps increases while the width of steps decreases. Figure 11 shows the density gradient profile of three solutions with initial density gradients (11(a)) $g_i = 4.3$, (11(b)) $g_i = 5.1$, and (11(c)) $g_i = 5.5$. In each solution, the density profile consists of three jumps. However, each solution arrives at its related profile from different evolution of paths. For the solution related to Fig. 11(a), with an initial density gradient of $g_i = 4.3$, at first four jumps form. After a merger between two of the steps, a snapshot of density gradient profile is taken at $t = 2$. For the solution in Fig. 11(b), initially fourteen jumps form in the system; after a much longer evolutionary time including ten mergers, at $t = 800$, a snapshot is taken from the profile. Note that this profile of the system is in the more advanced stage of spatial migration towards the left boundary. For the solution in Fig. 11(c), with $g_i = 5.5$, the maximum number of three jumps form, and this snapshot of the profile is taken at $t = 2$. Comparing the Figs. 11(a), 11(b), and 11(c) shows the width of the jumps increases with the value of the initial density gradient.

Large turbulence spreading wipes out features on smaller spatial scales in the mean field profiles, resulting in the formation of density and vorticity patterns with broader spatial scales. Thus, for the same set of initial conditions, the mode number of the linear instabilities which develops into staircases can be controlled via the turbulence spreading parameter β. Equation (A15) in the Appendix gives $m_{\max}$, the mode number cutoff for the linearly unstable modes which is inversely proportional to turbulence spreading

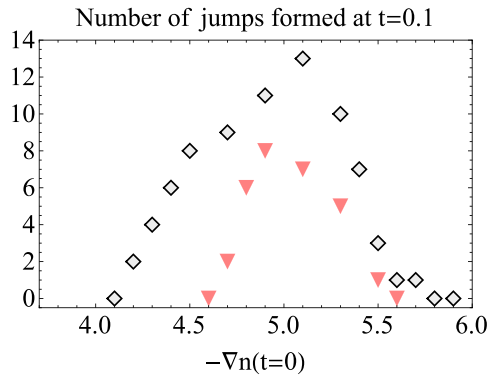

FIG. 10. Number of steps formed versus the initial density gradient $g_0 = -\partial_x n$, for two different viscosity values $\mu_c = 0.78$ (squares) and $\mu_c = 1.18$ (triangles).

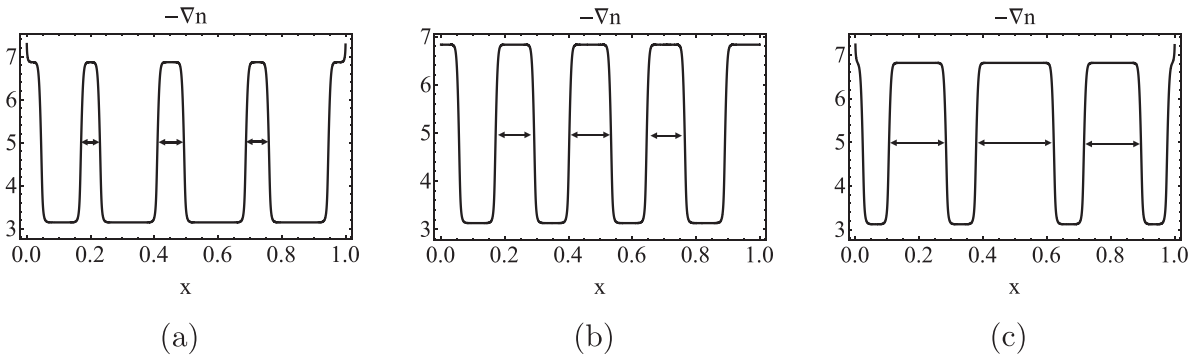

FIG. 11. Change in step width, with the change in the initial density gradient: (11(a)) $g_i = 4.3$, (11(b)) $g_i = 5.1$, and (11(c)) $g_i = 5.5$.

parameter β. Reducing β, increases $m_{\max}$, which results formation of more steps in the density profile. On the other hand, an increase in β will stabilize the high wave numbers, resulting in the development of features with smoother spatial variation. Our numerical results show that lower β results in the formation of more steps in the density profile, which emerges from the linear instabilities with higher mode numbers predicted by Eq. (A15) (see Fig. 12).

IV. FLUX DRIVEN EVOLUTION

In this section, we add an external particle flux drive to the density equation and use its amplitude Γ_0 (see Eq. (57)) as a control parameter. This flux drive source is chosen to be a peaked function at the origin. Our goal is to study: (i) the mean profile structure emerging from this dynamics (ii) transport bifurcation of the steady state (iii) variation with Γ_0 of the macroscopic steady state profiles of vorticity (i.e., shearing), density, turbulence, and particle flux and (iv) *global* and *local* flux-gradient landscapes.

For the density BC, at the origin, we choose the Neumann BC $(\partial_x n(x=0,t)=0)$, and Dirichlet BC on the outer boundary $n(x=1,t)=0$. The rest of the boundary conditions are $u(0,t)=u(1,t)=0$, $\partial_x \varepsilon(0,t)=\partial_x \varepsilon(1,t)=0$. Initial conditions for vorticity u and turbulent PE ε are identical to Section III. For the initial condition of the density, we choose a function of the form

$$n_0(x) = -g_i\left(x - 1 + \frac{1}{b}[e^{-bx} - e^{-b}]\right), \tag{55}$$

where we take $b=20$. This initial condition satisfies the chosen BCs for density. Moreover, away from the origin, the initial density gradient profile given by Eq. (55) is uniform and close to $-g_i$ (see Fig. 13 for an example of the initial density profile given by Eq. (55) with $g_i = 4.5$). The density equation with the flux drive is given by

$$\partial_t n = \partial_x\left[\left(\frac{l^2\varepsilon}{\alpha}\right)\partial_x n\right] + D_c\partial_x^2 n - \partial_x \Gamma_{\rm dr}(x). \tag{56}$$

We choose the following form for $\Gamma_{\rm dr}$

$$\Gamma_{\rm dr}(x) = \Gamma_0 \exp(-x/\Delta_{\rm dr}). \tag{57}$$

Γ_0 is the drive amplitude, and $\Delta_{\rm dr}$ is the width associated with the drive. In our solutions, we take $\Delta_{\rm dr} = 0.1$ as the constant. Dependence on alternative functional forms of flux drive, both in space and time will be studied in a future work. We can rewrite Eq. (56) as following:

$$\partial_t n = -\partial_x \Gamma_{\rm tot}; \quad \Gamma_{\rm tot}(x,t) = \Gamma(x,t) + \Gamma_{\rm dr}(x), \tag{58}$$

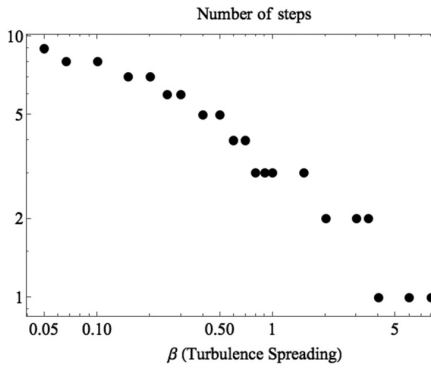

FIG. 12. Sharp decrease in the maximum number of the formed mesoscale steps versus the strength of turbulence spreading at early simulation times $t = 0.01$.

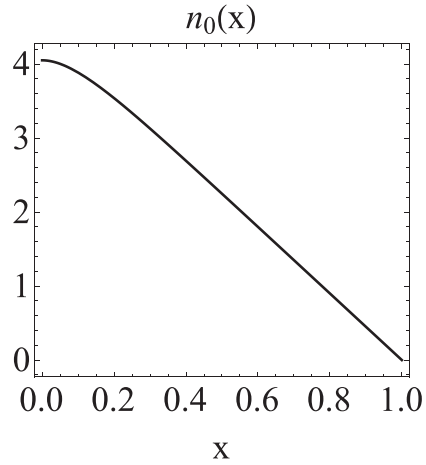

FIG. 13. Initial density profile given by the function $n_0(x)$ in Eq. (55) ($b = 20$), for $g_i = 4.5$.

where we defined $\Gamma(x,t)$ as the sum of the turbulent diffusion flux and the collisional diffusion flux

$$\Gamma(x,t) = -\left[\left(\frac{l^2\varepsilon}{\alpha}\right) + D_c\right]\partial_x n. \tag{59}$$

Thus with our choice of Neumann BC for n, the internal particle flux must satisfy the Dirichlet BC at $x=0$ (i.e., $\Gamma(0, t)=0$). As the solutions evolve to their final steady state, the total flux on the RHS of Eq. (58) saturates and becomes uniform. Thus, the steady *internal* particle flux Γ, defined in Eq. (59), must balance the external particle flux Γ_{dr}, and is given by

$$\Gamma(x) = \Gamma_{dr}(0) - \Gamma_{dr}(x). \tag{60}$$

$\Gamma(x)$ is a function of the steady solutions of $n(x), \varepsilon(x)$ and $u(x)$.

Figure 14 shows the development of system variables (n, u, and ε) from initial, to their final steady state, for constant values of drive amplitude (i.e., Γ_0), $\Gamma_2 = 6.84$ (Figs. 14(a), 14(b), and 14(c)) and $\Gamma_1 = 6.7$ (Figs. 14(d), 14(e), and 14(f)). The parameters chosen for this solution are $\beta = 0.1, \alpha = 4.5, \mu_c = 6, c_\chi = 0.9, \Lambda = 5000, \varepsilon_c = 2.2$ and we have taken the Prandtl number to be $Pr = \mu_c/D_c = 5$. For these values, a transport bifurcation of the steady-state takes place for $\Gamma_0 > \Gamma_{th} \approx 6.838$, and thus $\Gamma_1 < \Gamma_{th} < \Gamma_2$. For both Γ_1 and Γ_2, staircases form, with five jumps in the density profiles, in the early time of $t = 0.06$. For Γ_2, merger between the steps leads to the formation of the stationary macro-step at time $t \approx 20$, and at the location $x_{step} = 0.62$. Further raising of Γ_0 (beyond Γ_2) will move x_{step} to the left, resulting in a narrower step and higher density (n) at $x = 0$. However, for $\Gamma_1 < \Gamma_{th}$, the leftmost jump propagates to the right, and condensates and dissolves at $x = 1$. As a result, the steady solution for Γ_1 has no steady macro-step in its profile.

Transport bifurcation of the steady macro-state is shown in Fig. 15, by comparing the steady-state of the two solutions in Fig. 14, i.e., for Γ_1 and Γ_2. Figure 15(a) shows the rise in n with the formation of macro-step, and Fig. 15(b) depicts the drop in ε level in the density jump region ($x > 0.62$). Moreover, Fig. 15(d) shows a drop in the turbulent particle flux beyond x_{step} which implies that the steady macro-step acts as a *barrier* for the turbulent transport of particles. Furthermore, Fig. 15(c) shows the sign reversal of u for Γ_2 compared to Γ_1 (except in the close vicinity of $x = 0$) along with the enhancement of its amplitude. The characteristics of the macro-state solutions for $\Gamma_0 > \Gamma_{th}$ lead us to define these states as enhanced confinement modes (EC modes). In

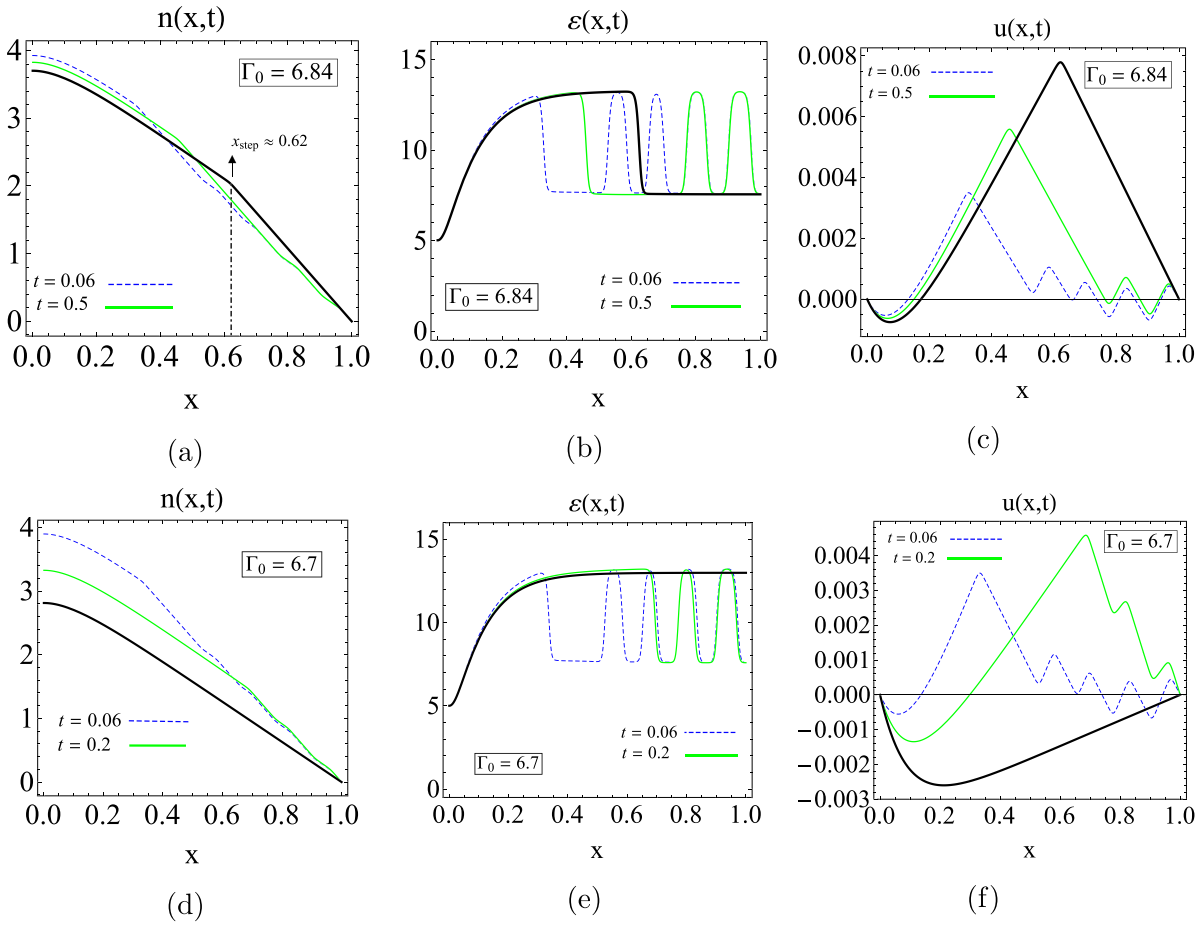

FIG. 14. Flux driven system with an initial density profile given by Fig. 13, for flux drive amplitudes $\Gamma_0 = 6.7 < \Gamma_{th}$ and $\Gamma_0 = 6.84 > \Gamma_{th}$, where the threshold flux amplitude for transition is $\Gamma_{th} = 6.838$. Parameters of the solutions are: $\beta = 0.1$, $\alpha = 4.5$, $\mu = 6$, $c_\chi = 0.9$, $\Lambda = 5000$, $\varepsilon_c = 2.2$, and $Pr = 5$.

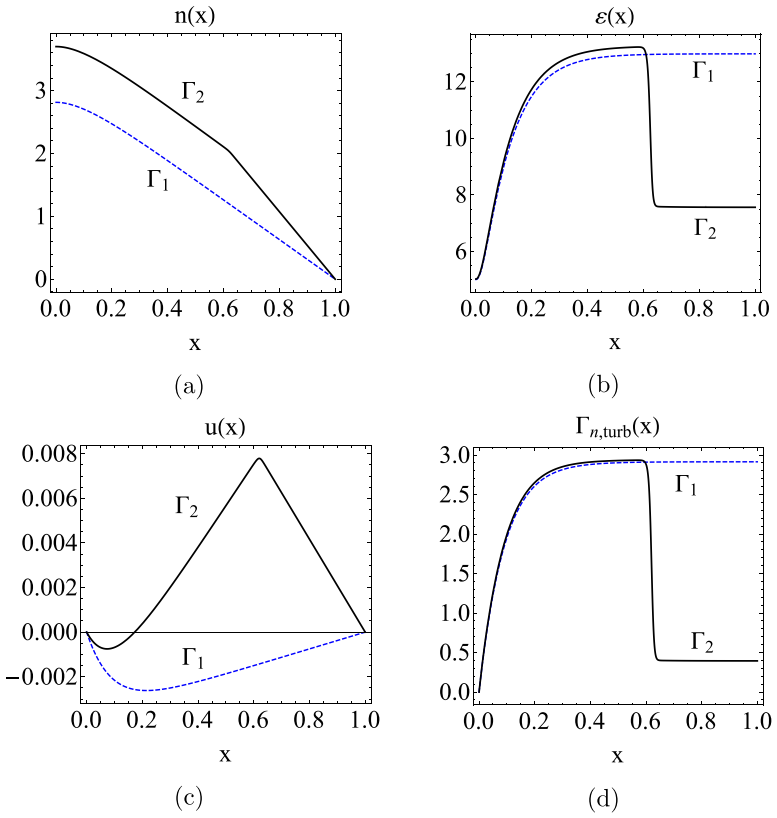

FIG. 15. Comparison between the final stationary profiles of two solutions with flux drive amplitudes $\Gamma_1 = 6.7$ and $\Gamma_2 = 6.84$, which are respectively below and above the threshold amplitude for transition $\Gamma_{th} \approx 6.838$.

contrast, the solutions for $\Gamma_0 < \Gamma_{th}$ are the normal confinement modes (NC modes).

The flux drive can build up the density gradient such that it would be large enough to undergo transport bifurcation. Therefore, a non-zero initial density gradient is not a necessary condition for the transport bifurcation of the steady macro-state. Figure 16 shows the evolution of the profiles for a system evolving from a flat density profile ($g_i = 0$), for two amplitudes of flux drive, both greater than the threshold of transition which for $g_i = 0$ is $\Gamma_{th} \approx 7.39$ (parameters of the system are identical to those of Fig. 15). The values of the flux amplitude are $\Gamma_0 = 7.4$ for Figs. 16(a), 16(b), and 16(c), which is very close to Γ_{th}, and a larger amplitude $\Gamma_0 = 10$ for Figs. 16(d), 16(e), and 16(f). With these values of Γ_0, a transport bifurcation takes place in the system which results in the formation of a barrier in the density profile. The density profile in Fig. 16(a) evolves smoothly from $t = 0$ to $t \approx 3$. This evolving density profile has a maximum gradient at the right boundary of the system ($x = 1$). As the density grows, so does its gradient and at $t \approx 3$, the value of the density gradient reaches a value for which the profile becomes linearly unstable. This instability starts from $x = 1$, develops to a step-jump form and moves towards left. The reason that only one step-jump forms, (instead of a staircase) is due to the fact that the density gradient profile becomes *locally* unstable, (in the immediate vicinity of $x = 1$), while the rest of the system is still stable. If the density gradient grows uniformly over a large range, then it will be possible for a multi-step staircase feature to form. For example, since the density profile in Fig. 13 has a uniform gradient for $x \gtrsim 0.3$, solutions that use this profile as their initial condition exhibit the multi-step staircase formation in Fig. 14. At $t \approx 8$ the profile reaches its stationary state with the final position of the step at $x_{step} \approx 0.26$. Moreover, in the profile for turbulent PE (Fig. 16(b)), at the time of transition $t \approx 3$, the right side of the ε profile drops; propagates to the left, and comes to stop at the stationary position $x_{step} \approx 0.26$.

Figures 16(d), 16(e), and 16(f) show the development of profiles to their steady macro-state for $\Gamma_0 = 10$, which is further above $\Gamma_{th} \approx 7.39$. Figure 16(d) shows that as the profile develops, the steepest point is at $x \approx 0.27$ (which can be seen on the $t = 0.13$ curve), and as a result, step forming instability starts from this location. At time $t = 0.22$, and at $x \approx 0.27$, a jump develops in the density profile. As time goes on, this jump broadens and develops into the steady state barrier (full black curve); barrier position is at $x_{step} \approx 0.12$. Further increasing Γ_0 will result in further displacement of x_{step} to the left. In the limit of $\Gamma \gg 1$, x_{step} approaches the left boundary ($x_{step} \to 0$).

A. Mean flux-gradient relation and landscape

Transport bifurcation in the *global* flux-density relation of the system appears as a gap in the unstable regions of global variables (i.e., radially averaged flux and density), as the steady-state radial profiles of system variables undergo drastic transformations. The global particle flux-density gradient relation of the steady macro states is mapped in Fig. 17. These data points are the results of individual solutions

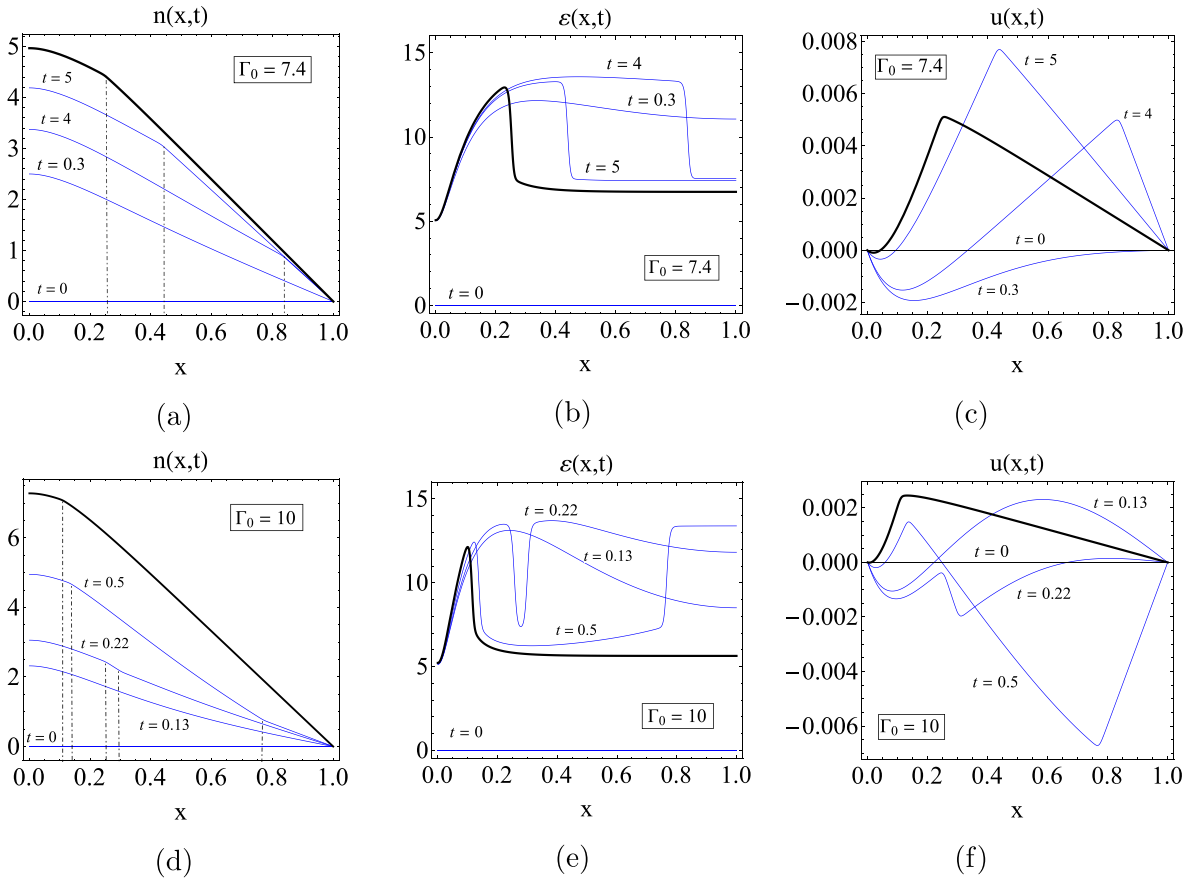

FIG. 16. Evolution of variables of a flux driven system, starting from an initially flat density profile, for flux drive amplitudes of $\Gamma = 7.4$ in 16(a), 16(b), and 16(c), and for flux drive amplitudes of $\Gamma = 10$ in 16(d), 16(e), and 16(f). Both of the flux amplitudes are above the threshold amplitude of transition $\Gamma_{th} \approx 7.39$, and as a result for both solutions, a stationary barrier forms.

at a constant Γ_0, which evolve into their steady state. Diamonds represent solutions with initially flat density gradient ($g_i = 0$), and triangles represent solutions with initial density profile given by Fig. 13 ($g_i = 4.5$). The vertical and the horizontal axes are, respectively, the radially averaged $\Gamma(x)$ and $-\partial_x n$. With the assumed choice of a Dirichlet BC for the density at $x = 1$ (i.e., $n(1, t) = 0$), for $\langle -\partial_x n \rangle$ we get

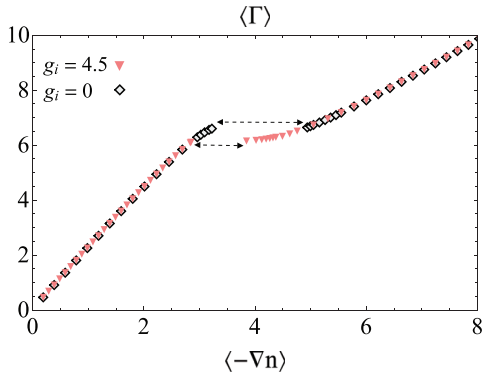

FIG. 17. Volume averaged particle flux versus the volume averaged density gradient for the final stationary state of the system.

$$\langle -\partial_x n \rangle = \int_0^1 [-\partial_x n(x,t)] dx = n(0,t). \tag{61}$$

Moreover, since the steady state particle flux is given by Eq. (60), the spatially averaged flux is given by

$$\langle \Gamma \rangle = \int_0^1 \Gamma(x) dx = \Gamma_0 [1 - \Delta_{dr}(1 - e^{-1/\Delta_{dr}})]. \tag{62}$$

Equation (62) shows that $\langle \Gamma \rangle$ is a linearly increasing function of Γ_0. Moreover, Fig. 17 shows that $\langle -\partial_x n \rangle$ is a monotonically increasing function of Γ_0. There are two gaps in the steady solutions (shown by double headed arrows). Solutions with values of $(\langle -\partial_x n \rangle, \langle \Gamma \rangle)$ in these gaps are linearly unstable (see Eq. (49)). As a result, steady state solutions cannot exist within the gaps. By raising Γ_0, the value of $\langle \Gamma \rangle$ increases continuously and the gap in the data manifests as a jump in $\langle -\partial_x n \rangle$, as a result of a global transport bifurcation. Solutions on the right side of the gap are EC states, and solutions on the left side of the gap are NC states. Away from the gaps, the $(\langle -\partial_x n \rangle, \langle \Gamma \rangle)$ values of the solutions with $g_i = 4.5$ and $g_i = 0$ overlap.

While the global flux-gradient diagram exhibits the global transport bifurcation in the system, the local flux-gradient

relation (i.e., as a function of radius) shows how the variables at different radial locations behave, as this transition occurs. Figure 18 gives the *local* landscape of $\Gamma(x)$ versus $-\partial_x n$ versus x for $g_i = 4.5$. Each curve in the plot is the steady solution for a constant value of Γ_0. ECs form for $\Gamma_0 \gtrsim \Gamma_{th} = 6.838$ and are shown in shades of red. NC form for $\Gamma_0 < \Gamma_{th}$ and are depicted in gray scale. Projection of these curves on the $\partial_x n = 0$ plain gives the $\Gamma(x)$ versus x dependence described by Eq. (60), as the value of Γ_0 is raised. In addition, projection of these curves on $\Gamma = 0$ gives the steady profiles of the density gradient $-\partial_x n$ versus x. At Γ_{th} the location of the barrier step x_{step} is the farthest to the right at $x \approx 0.65$, and as Γ_0 is raised, x_{step} moves to the left. As a result, a gap exists in the data set which is pointed out with a dashed rectangle for $x > 0.65$ and $\Gamma \approx 6.838$.

B. Hysteresis in flux-gradient relation

The global flux-gradient relation of the system can exhibit hysteresis as the flux drive amplitude Γ_0 is first raised, and then lowered, in one parameter scan run. Time variation of Γ_{dr} is adiabatic, so that at all times, the system is close to a steady state solution, except for the short transition times. The functional form of Γ_{dr} is the same as Eq. (60), as Γ_0 varies with time. From $t = 0$ to $t = 10$, Γ_0 is kept at a constant, so that during this time, the system variables evolve and reach the steady state. From $t = 10$ to $t = 1010$, flux amplitude grows linearly from $\Gamma_0 = 6$ to $\Gamma_0 = 8$, and from $t = 1010$ to $t = 2010$, the flux amplitude decreases linearly from $\Gamma_0 = 8$ to $\Gamma_0 = 6$.

Figure 19 shows the flux-gradient relation of the process described above. Two different transitions can occur. The forward transition (FT) occurs for $\Gamma_0 = \Gamma^f_{th} \approx 7.39$, as Γ_0 is increased, and the backward transition (BT) occurs for $\Gamma_0 = \Gamma^b_{th} \approx 6.838$, as Γ_0 is decreased. Critical transition points along the hysteresis loop are noted (**A**, **B**, **C**, and **D**). The **A**-**B**, and **C**-**D** gaps result from the transport bifurcation,

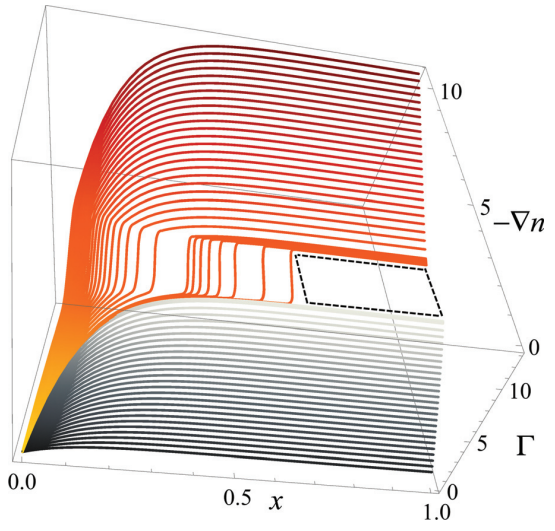

FIG. 18. Flux landscape of the local $\Gamma(x)$ versus $-\partial_x n$ versus x for $g_i = 4.5$. Shades of red are for the enhanced confinement states (EC) and gray scale is for the normal confinement state (NC). Lighter or brighter shades are used to accentuate the three-dimensional sense and do not represent a varying physical quantity.

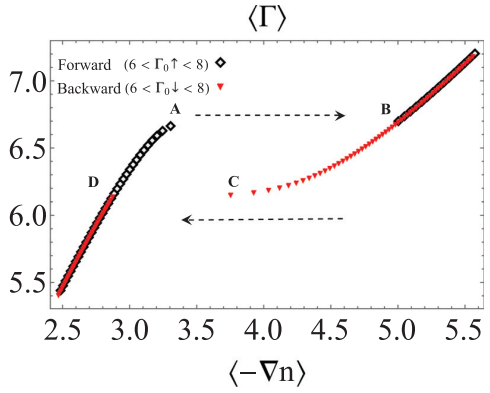

FIG. 19. Global particle flux versus density gradient, showing hysteresis behavior. Reprinted with permission from Ashourvan and Diamond, Phys. Rev. E **94**, 051202(R) (2016). Copyright 2016 American Physical Society.[36]

leading, respectively, to barrier formation in the FT, and barrier annihilation in BT. The loop formed due to the separation between the FT and the BT, results from transport bifurcation taking place at different values of Γ_{th} in each direction. This loop is a clear evidence for hysteresis behavior in this process.

Fig. 20 shows the transformation of the steady-state profiles at the critical transition points of Fig. 19. Curves labeled **A** and **B** are snapshots of the profiles for which Γ_0 is, respectively, slightly below and slightly above Γ^f_{th}, i.e., $\Gamma_0|_{\mathbf{A}} \lesssim \Gamma^f_{th} \lesssim \Gamma_0|_{\mathbf{B}}$ (in the BT, $\Gamma_0|_{\mathbf{D}} \lesssim \Gamma^b_{th} \lesssim \Gamma_0|_{\mathbf{C}}$). During these fast transitions, (shown in blue solid arrows), the system is not in steady-state. From **B** to **C**, as Γ_0 is raised from Γ^f_{th} to 8 and then lowered to Γ^b_{th}, the barrier position x_{step} gradually, first moves from $x_{step} \approx 0.26$ to $x_{step} \approx 0.24$, and then moves to $x_{step} \approx 0.65$. Finally, the transition from EC (curve **C**) to NC (curve **D**) occurs at Γ^b_{th}. The timescale for this transition is $\Delta_{CD} \sim 10$. During this time, while x_{step} moves from $x \approx 0.65$ to $x = 1$, height of the barrier decreases to zero.

V. DISCUSSION AND CONCLUSION

The HW DW-turbulence system is extensively studied and conserves both the energy and potential enstrophy up to dissipation terms. In our model, the total PE conservation is a central feature in the evolution of profiles. More specifically, it is the mixing of potential vorticity that regulates the interaction between the mean fields and the turbulence through an internal turbulence production term which converts the mean PE to fluctuation PE. The model uses a dynamic mixing length which is a nonlinear function of the Rhines scale l_{Rh}. As a result, through its l_{Rh} dependence, the mixing length is a nonlinear function of the PV gradient. The choice of mixing length is a crucial element of this model, which closes the positive feedback-loop on PV. This feedback loop results in local transport bifurcations due to inhomogeneous mixing of PV. As a result, nonlinear features form in the mean profiles. These nonlinear structures are the density staircases and the shear lattice patterns and transport barriers. Hence, our reduced turbulence model of two coupled mean fields exhibits results which are similar to both the spontaneous layering in a stratified fluid in Ref. 33, and

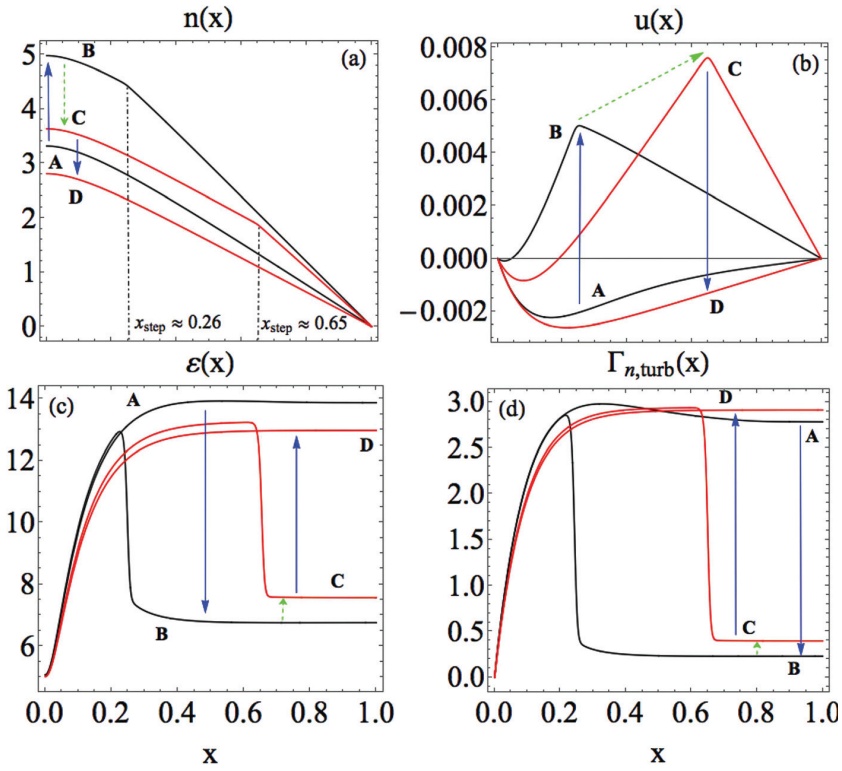

FIG. 20. Transformation in the profiles of (15a) density, (15b) vorticity, (15c) turbulent PE, and (15d) turbulent particle flux. Forward transition is from **A** to **B**, and backward transition is from **C** to **D**. Reprinted with permission from Ashourvan and Diamond, Phys. Rev. E **94**, 051202(R) (2016). Copyright 2016 American Physical Society.[36]

the formation and sharpening of jet shear layers in planetary atmospheres in Refs. 4, 6, and 10. Indeed, in this system, the two layerings occur together and are closely related. The density staircase is similar to the buoyancy field layering while the shear jumps resemble the jet staircase. Of course here, shear jumps support the density corrugations.

By numerically solving the nonlinear system of equations of our reduced model, we study the evolution of the mean and turbulence fields from their initial values. Here is a summary of our results:

(i) Structure formation is observed and proceeds through (roughly) three different evolutionary stages:
   (1) In the first stage, the nonlinear quasi-periodic features in density and vorticity profile develop from the (linear) secondary modulational instabilities (primary instabilities are the DWs). The staircase features locally reorganize and transform through the process of merger which reduces the roughness of the overall pattern, resulting in the formation of mesoscale staircases and shear lattices.
   (2) In the second stage of evolution, local transformation of profiles through merger continues. As the spatial scale of the structures grows, mergers become less frequent and eventually stop.
   (3) In the third stage of evolution, the structures in density and vorticity profile detach from their locations of formation and propagate (or migrate) towards the boundaries. When the steps in the staircase structure and shear layers reach the boundaries, they condense and are sometimes absorbed into the boundaries. The migration process continues until the final steady macro-barriers form. This process occurs in a much longer time - about two orders of magnitude larger than that of the first two stages.

(ii) The number of jumps and steps formed in a staircase in its early evolutionary stage is sensitive to the initial PV gradient, g_i. As seen in Fig. 10, with increasing g_i from small to large values, the number of steps increases from zero to a maximum value, and then decreases to zero, again.

(iii) Spreading of turbulent PE is found to be necessary in the formation of structures as it regulates the steepening in the ε profile. Eq. (A15) shows that the maximum wave number for the feature forming instabilities is inversely proportional to β, the coefficient controlling the strength of turbulent PE spreading. Results of numerical simulation show that lowering β results in the formation of more steps and jumps in the density profile. Moreover, below a critical value of β, the numerical solutions become too stiff, due to the very fine spatial scale of instabilities and extreme local steepening of gradients. On the other hand, raising β results in the formation of smaller number of jumps-steps in the staircase profiles. In the extreme case of large β, the turbulent spreading of PE prevents the formation of any spatial structures in the mean fields.

(iv) The steady macro-state of a system driven by an external particle flux undergoes a transport bifurcation, from a normal confinement (NC) state to an enhanced confinement state (EC), as the amplitude of the flux drive is increased beyond a threshold for

transition Γ_{th}. The density profile of the EC state is one of a step (flattened profile) in the inner region, located adjacent to a jump (steepened profile) at the edge. NC density profile is smooth, with no jump-step features. As Γ_0 is increased above Γ_{th}, and at the transition from NC to EC, the value of the density at the axis ($x=0$) discontinuously increases to a higher value. For the EC state, in the outside "jump" region, the level of turbulent PE as well as the turbulent particle flux drop, in comparison to these levels in the inside "step" region. With the transition from NC to EC state, the shearing profile changes sign except in the close vicinity of the axis. Also the amplitude of the shearing increases as the result of this transition (see Fig. 15 for examples of EC (solid curves) and NC (dashed curves) profiles of mean density, mean vorticity, turbulent PE, and turbulent particle flux).

(v) The global particle flux versus the density gradient relation exhibits hysteresis: While raising Γ_0 adiabatically in time, the forward transition from NC to EC takes place at $\Gamma_0 = \Gamma^f_{th}$. Decreasing the flux drive will result in a transition from NC to EC, at $\Gamma_0 = \Gamma^b_{th} < \Gamma^f_{th}$. Difference in paths the system takes for the forward and backward transition results in the formation of a hysteresis loop in the global particle flux versus the density gradient relation of the macro-state.

The reduced model presented here exhibits the global emergence of quasi-periodic mesoscale density staircase structures, colocated with a shearing lattice, and the evolution of these meso structures to the macro steady state. Moreover, the numerical simulation results are sensitive to the boundary conditions, and the choice of BC can drastically impact the results.

The simplicity of this reduced model facilitates its extension to more complex scenarios such as the ITG/TEM-ETG turbulence system. This task can be carried out by inclusion of other mean fields such as the electron and ion temperatures, as well as a second population of turbulence which interacts with the mean fields and the first turbulence population. The aim, there, would be, to understand staircases in other fields such as ion and electron temperatures, and to examine the possible spatial phase lags between them, resulting from multi-scale interactions.

ACKNOWLEDGMENTS

This research was supported by the U.S. Department of Energy Grant Nos. DE-FG02-04ER54738, and DE-SC0008378 and CMTFO. We thank G. Dif-Pradalier, Y. Kosuga, Ö. D. Gürcan, M. Malkov, D. W. Hughes, and G. R. Tynan for useful discussions. The authors thank the participants in the 2015 Festival de Theorie, (Aix-en-Provence, France) for many stimulating discussions.

APPENDIX: LINEAR INSTABILITY CONDITIONS FOR THE PV PROFILE

Here, we analyze the stability of the equilibrium of the PV and PE system.[33] First we rewrite these equations as

$$g_t = G_{xx}, \quad \varepsilon_t = [\sigma \varepsilon_x]_x + p, \tag{A1}$$

where $g = -\partial_x q$ and

$$G = \frac{c_\chi \varepsilon}{\alpha(1+g^2/\varepsilon)^\kappa} g + \mu g, \tag{A2}$$

$$p = \frac{c_\chi \varepsilon}{\alpha(1+g^2/\varepsilon)^\kappa} g^2 - \frac{\varepsilon^{3/2}}{\varepsilon_0^{1/2}} + \varepsilon, \tag{A3}$$

$$\sigma = \beta \frac{\varepsilon^{1/2}}{(1+g^2/\varepsilon)^\kappa}. \tag{A4}$$

The equilibrium solution satisfies

$$p(g_0, \varepsilon_0) = 0, \quad G(g_0, \varepsilon_0) = \Gamma_q(g_0). \tag{A5}$$

From the above equation, we obtain the following relation for the flux gradient function:

$$\Gamma'_q(g_0) = (p_\varepsilon G_g - p_g G_\varepsilon)/p_\varepsilon, \tag{A6}$$

where all the partial derivatives are evaluated for the equilibrium values g_0 and ε_0. Now we assume the linear perturbations of the form

$$g = g_0 + \delta g \exp(st + imx), \quad \varepsilon = \varepsilon_0 + \delta\varepsilon \exp(st + imx). \tag{A7}$$

Substituting from Eq. (A7) in Eq. (A1), we obtain the linearized equations as

$$s\delta g = -m^2(f_g \delta g + f_\varepsilon \delta\varepsilon), \tag{A8}$$

$$s\delta\varepsilon = -m^2\sigma\delta\varepsilon + p_\varepsilon \delta\varepsilon + p_g \delta g. \tag{A9}$$

Above equations result in the following equation for s:

$$s^2 + [m^2(\sigma + G_g) - p_\varepsilon]s - m^2\Gamma'_q p_\varepsilon + m^4 \sigma f_g = 0. \tag{A10}$$

Marginally stable solutions are obtained for $s \approx 0$. From Eq. (A10), these solutions are obtained for

$$m^2 \approx 0, \tag{A11}$$

$$m^2 = p_\varepsilon \Gamma'_q / \sigma f_g. \tag{A12}$$

For $m^2 \approx 0$, we solve for s to obtain

$$s \approx -m^2 \Gamma'_q, \quad (\delta g, \delta\varepsilon) \approx (1, -p_g/p_\varepsilon). \tag{A13}$$

From the above equation, we can see that in order for the modes to be unstable ($s > 0$) we must have

$$\Gamma'_q(g_0) < 0. \tag{A14}$$

Moreover Eq. (A12) gives the maximum wave number for the unstable modes

$$m^2_{max} = p_\varepsilon \Gamma'_q / \sigma f_g. \tag{A15}$$

[1]R. Waltz, M. Austin, K. Burrell, and J. Candy, Phys. Plasmas **13**, 052301 (2006).
[2]J. E. Kinsey, G. M. Staebler, K. H. Burrell, and R. E. Waltz, Phys. Rev. Lett. **86**(5), 814 (2001).

[3]P. H. Diamond, S.-I. Itoh, K. Itoh, and T. S. Hahm, Plasma Phys. Controlled Fusion **47**, R35–R161 (2005).
[4]D. G. Dritschel and M. E. McIntyre, J. Atmos. Sci. **65**, 855 (2008).
[5]C. W. Hughes, J. Phys. Oceanogr. **26**, 1375–1387 (1996).
[6]P. S. Marcus, Annu. Rev. Astron. Astrophys. **31**, 523 (1993).
[7]L. D. Landau, E. M. Lifshitz, A. M. Kosevich, and L. P. Pitaevskii, *Theory of Elasticity* (Elsevier, 1986).
[8]O. M. Phillips, Deep Sea Res. **19**, 79 (1972).
[9]B. R. Ruddick, T. J. McDougall, and J. S. Turner, Deep-Sea Res. **36**, 597–609 (1989).
[10]M. N. Juckes and M. E. McIntyre, Nature **328**, 590–596 (1987).
[11]G. Dif-Pradalier, P. Diamond, V. Grandgirard, Y. Sarazin, J. Abiteboul, X. Garbet, P. Gendrih, A. Strugarek, S. Ku, and C. S. Chang, Phys. Rev. E **82**, 025401(R) (2010).
[12]G. Dif-Pradalier, G. Hornung, P. Gendrih, Y. Sarazin, F. Clairet, L. Vermare, P. Diamond, J. Abiteboul, T. Cartier-Michaud, C. Ehrlacher, D. Esteve, X. Garbet, V. Grandgirard, Ö. D. Gürcan, P. Hennequin, Y. Kosuga, G. Latu, P. Maget, P. Morel, C. Norscini, R. Sabot, and A. Storelli, Phys. Rev. Lett. **114**, 085004 (2015).
[13]E. Kim and P. H. Diamond, Phys. Plasmas **9**, 4530 (2002).
[14]R. Waltz, G. Kerbel, and J. Milovich, Phys. Plasmas **1**, 2229 (1994).
[15]W. Dorland and G. Hammett, Phys. Fluids B **5**, 812 (1993).
[16]M. A. Beer, *Gyrofluid Models of Turbulent Transport in Tokamaks* (Princeton University, Department of Astrophysical Sciences, 1995).
[17]B. N. Rogers, W. Dorland, and M. Kotschenreuther, Phys. Rev. Lett. **85**, 5336 (2000).
[18]S. Kobayashi and B. N. Rogers, Phys. Plasmas **19**, 012315 (2012).
[19]E. Kim and P. H. Diamond, Phys. Plasmas **10**, 1698 (2003).
[20]L. Schmitz, L. Zeng, T. L. Rhodes, J. C. Hillesheim, E. J. Doyle, R. J. Groebner, W. A. Peebles, K. H. Burrell, and G. Wang, Phys. Rev. Lett. **108**, 155002 (2012).
[21]G. Tynan, M. Xu, P. H. Diamond, J. A. Boedo, I. Cziegler, N. Fedorczak, P. Manz, K. Miki, S. Thakur, L. Schmitz, L. Zeng, E. J. Doyle, G. M. McKee, Z. Yan, G. S. Xu, B. N. Wan, H. Q. Wang, H. Y. Guo, J. Dong, K. Zhao, J. Cheng, W. Y. Hong, and L. W. Yan, Nucl. Fusion **53**, 073053 (2013).
[22]L. A. Charlton, B. A. Carreras, V. E. Lynch, K. L. Sidikman, and P. H. Diamond, Phys. Plasmas **1**, 2700 (1994).
[23]A. Hasegawa and M. Wakatani, Phys. Rev. Lett. **59**, 1581 (1987).
[24]M. Wakatani and A. Hasegawa, Phys. Fluids **27**, 611 (1984).
[25]P. N. Guzdar, J. F. Drake, D. McCarthy, A. B. Hassam, and C. S. Liu, Phys. Fluids B **5**, 3712 (1993).
[26]H. Sugama, M. Wakatani, and A. Hasegawa, Phys. Fluids **31**, 1601 (1988).
[27]B. Carreras, V. E. Lynch, and L. Garcia, Phys. Fluids B **5**, 1795 (1993).
[28]B. D. Scott, Plasma Phys. Controlled Nucl. Fusion Res. **III**, (Vienna: IAEA) 447 (1995).
[29]V. Naulin, Phys. Plasmas **10**, 4016 (2003).
[30]A. Ashourvan, P. H. Diamond, and Ö. D. Gürcan, Phys. Plasmas **23**, 022309 (2016).
[31]P. H. Diamond, D. W. Hughes, M. A. Malkov, G. Dif-Pradalier, O. D. Gurcan, G. T. Katt, and Y. Kosuga, "Staircase Formation and Avalanching in Plasmas and Fluids" (to be published).
[32]M. Malkov and P. H. Diamond, "Dynamics of staircase formation and evolution in a reduced model of beta plane turbulence" (to be published).
[33]N. J. Balmforth, S. G. Llewellen-Smith, and W. R. Young, J. Fluid Mech. **355**, 329–358 (1998).
[34]Y. Kosuga, P. H. Diamond, and Ö. D. Gürcan, Phys. Rev. Lett. **110**, 105002 (2013).
[35]Y. Kosuga, P. H. Diamond, G. Dif-Pradalier, and Ö. D. Gürcan, Phys. Plasmas **21**, 055701 (2014).
[36]A. Ashourvan and P. H. Diamond, Phys. Rev. E **94**, 051202(R) (2016).